

Organoid models of breathing disorders reveal patterning defect of hindbrain neurons caused by PHOX2B-PARMs

Kathy Nga-Chu Lui,¹ Zhixin Li,¹ Frank Pui-Ling Lai,¹ Sin-Ting Lau,¹ and Elly Sau-Wai Ngan^{1,*}

¹Department of Surgery, Li Ka Shing Faculty of Medicine, The University of Hong Kong, Pokfulam, Hong Kong SAR

*Correspondence: engan@hku.hk

<https://doi.org/10.1016/j.stemcr.2023.05.020>

SUMMARY

Retrotrapezoid nucleus (RTN) neurons in the brainstem regulate the ventilatory response to hypercarbia. It is unclear how PHOX2B-polyalanine repeat mutations (PHOX2B-PARMs) alter the function of PHOX2B and perturb the formation of RTN neurons. Here, we generated human brainstem organoids (HBSOs) with RTN-like neurons from human pluripotent stem cells. Single-cell transcriptomics revealed that expression of PHOX2B+7Ala PARM alters the differentiation trajectories of the hindbrain neurons and hampers the formation of the RTN-like neurons in HBSOs. With the unguided cerebral organoids (HCOs), PHOX2B+7Ala PARM interrupted the patterning of PHOX2B+ neurons with dysregulation of Hedgehog pathway and *HOX* genes. With complementary use of HBSOs and HCOs with a patient and two mutant induced pluripotent stem cell lines carrying different polyalanine repetition in PHOX2B, we further defined the association between the length of polyalanine repetition and malformation of RTN-respiratory center and demonstrated the potential toxic gain of function of PHOX2B-PARMs, highlighting the uniqueness of these organoid models for disease modeling.

INTRODUCTION

Ventilatory responses to hypoxia and hypercapnia are regulated by a specific set of chemoreceptors and motor neurons in the hindbrain. Retrotrapezoid nucleus (RTN) is a major center of chemoreceptors in the ventrolateral medulla that provides excitatory drives to the central respiratory pattern generator. It comprises a bilateral cluster of carbon dioxide (CO₂)-sensitive glutamatergic neurons that express vesicular-glutamate transporter-2 (VGLUT2) and homeobox transcription factor PHOX2B (Goridis et al., 2010; Guyenet et al., 2019). These glutamatergic RTN neurons not only detect the CO₂ level in the brain but also integrate chemosensory information from chemoreceptors, where innervating serotonin (5-HT) neurons enhance their chemosensitivity (Moreira et al., 2016). In response to elevated CO₂ levels, RTN neurons intermingle with C1 neurons to excite A5 neurons and stimulate breathing and increase the rhythmic pattern of respiratory activity (Guyenet et al., 2005). This RTN-mediated central respiratory chemoreflex provides an important respiratory stimulus during apnea and dyspnea.

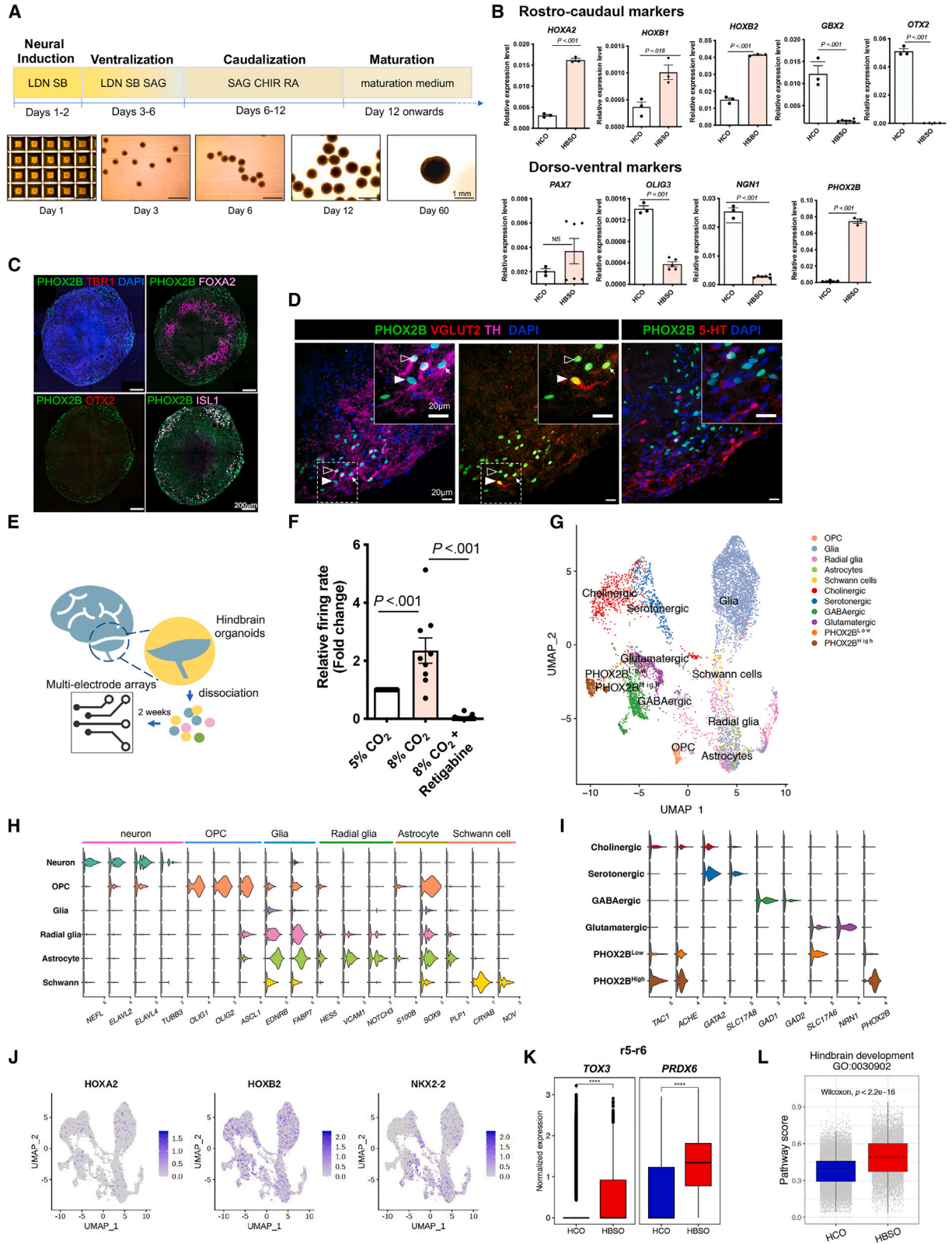
Congenital central hypoventilation syndrome (CCHS) is a life-threatening disease caused by the loss of RTN neurons in the brainstem. It is characterized by inadequate autonomic control of breathing due to impaired ventilatory response to hypercarbia and hypoxemia (Dubreuil et al., 2008). Polyalanine repeat expansion mutations (PARMs), resulting in +5 to +13 additional alanine (Ala) residues in the 20-residue polyalanine tract of PHOX2B, are highly associated with CCHS, where longer polyalanine repetition is asso-

ciated with more severe disease phenotypes (Amiel et al., 2003; Bachetti and Ceccherini, 2020; Matera et al., 2004).

Mouse mutants carrying +7Ala-PARM in *Phox2b* lack Phox2b⁺ RTN neurons but have enriched Phox2b⁺ glutamatergic neurons on the dorsal side of facial nucleus (nVII). These mutants exhibit CCHS-like phenotypes including breathing defects, absence of response to hypercapnia, and death from central apnea soon after birth (Dubreuil et al., 2008, 2009). Several attempts have been made to establish hindbrain (Butts et al., 2019) or brainstem (Eura et al., 2020) organoids using human pluripotent stem cells (hPSCs). Nevertheless, these protocols did not provide cues for the generation of functional RTN neurons and thus hampered their application in disease modeling for CCHS. It remains unclear how PARMs affect the functions of PHOX2B and the formation of RTN neurons in the brainstem and whether longer PARMs lead to more severe CNS defects.

In this project, we generated hPSC-based brainstem (HBSO) and cerebral (HCO) organoids with cytoarchitectures resembling the RTN-respiratory center. We then unveiled the molecular mechanisms underlying PHOX2B-PARMs on the development of hindbrain neurons through analyzing the single-cell transcriptomes of HBSOs and HCOs derived from a PHOX2B +7Ala-PARM hPSC line. Proof-of-concept studies were also conducted with additional mutant hPSC lines carrying different lengths of PARMs and a CCHS-patient-specific hPSC line to illustrate the potential applications of these organoid models for recapitulating the PARM-associated RTN defects *in vitro*.





(legend on next page)



RESULTS

Generation and characterization of human brainstem organoids from hPSCs

To develop an *in vitro* human model of CCHS, we first used a control hPSC cell line (UE02306) to establish a differentiation protocol for the generation of HBSOs with enriched PHOX2B⁺ and RTN neurons. RTN neurons originate from the rhombomere 5 (r5) and dB2 domains, which require WNT and retinoic acid (RA) signaling during development (Guyenet et al., 2019). Therefore, after directing the hPSCs to neural cell fate by dual-SMAD inhibitors (LDN193189 and SB431542) and ventralization by SHH agonist (SAG), the spheroids were caudalized to hindbrain cell fate with WNT agonist (CHIR99021) and RA (Figure 1A). Compared with HCOs comprising different subregions of the brain generated from an unguided differentiation protocol (Giandomenico et al., 2021; Lancaster and Knoblich, 2014; Lancaster et al., 2013), HBSOs expressed significantly higher levels of r4-5 markers (*HOXA2*, *HOXB1*, and *HOXB2*) but lower levels of r1 marker (*GBX2*) and undetectable levels of midbrain marker (*OTX2*) by day 20 of differentiation (Figure 1B). Regarding the dorsal-ventral specification, HBSOs expressed a much higher level of *PHOX2B* but lower levels of *OLIG3* and *NGN1* than HCOs while retaining the *PAX7* expression (Figure 1B). This implies HBSOs have a spatial identity similar to the dB2 domain but not the other two PHOX2B⁺ domains (i.e., dA3 and MNv).

By day 60, most of the PHOX2B⁺ cells in the HBSOs retained specific position codes for hindbrain neurons, co-ex-

pressing the hindbrain marker (*ISL1*) but not the midbrain (*OTX2/FOXA2*) or the forebrain (*TBR1*) markers (Figure 1C). In addition, PHOX2B⁺ glutamatergic RTN-like (PHOX2B⁺; VGLUT2⁺; TH⁻) neurons were residing near to A5-(PHOX2B⁺; TH⁺; VGLUT2⁻), C1- (PHOX2B⁺; TH⁺; VGLUT2⁺) and 5-HT⁺ neurons, resembling the respiratory center of the brainstem (Figure 1D). We then assessed the potential hypercapnia response of HBSO neurons by performing multielectrode array (MEA) analyses. Dissociated HBSO neurons were plated onto an MEA plate for 1–2 weeks for network re-establishment (Figure 1E), and the neural activity was then measured under different CO₂ levels (5% or 8%). Increased firings were detected in response to the elevated CO₂ level, and that was blocked by an RTN-specific blocker (retigabine) (Hawryluk et al., 2012) (Figure 1F), suggesting the presence of hypercapnia-responsive RTN neurons in the HBSOs.

scRNA-seq analyses reveal cell type diversity and hindbrain molecular signatures of HBSOs

To further investigate the cellular composition and molecular signatures of HBSOs, we performed single-cell transcriptomic analyses of day-60 HBSOs and compared with the HCOs derived from the same control hPSC line. A total of 11,347 cells from a pool of >20 HBSOs and 42,970 cells from a pool of eight HCOs were sequenced using 10X Genomics, with 2,319 median genes and 24,389 mean unique molecular identifiers detected per cell (Figure S1A). All single cells were projected onto Uniform Manifold Approximation and Projection (UMAP) plots, and single-cell RNA-sequencing (scRNA-seq) datasets of hindbrain cells

Figure 1. Generation and characterization of brainstem organoids (HBSOs)

- (A) Schematic showing the derivation of HBSOs from hPSCs. Representative phase-contrast images showing the HBSOs derived from the control hPSCs at different stages of differentiation.
- (B) qRT-PCR analyses show the relative expressions of rostro-caudal (*HOXA2*, *HOXB1*, *HOXB2*, *GBX2*, and *OTX2*) and dorsoventral (*PAX7*, *OLIG3*, *NGN*, and *PHOX2B*) markers in the day-20 control HBSOs in comparison to the day-60 HCOs. Data are represented as mean ± SEM of three independent pools of ≥ 4 organoids. Unpaired t test; NS, non-significant.
- (C) Immunostaining of PHOX2B and markers of the forebrain (*TBR1*), midbrain (*FOXA2*, *OTX2*), and hindbrain (*ISL1*) in the day-60 control HBSOs.
- (D) Immunostaining of PHOX2B, TH, VGLUT2, and 5-HT in the day-60 control HBSOs. The inset on the top-right corner is an enlargement of a square region in the image. RTN (PHOX2B⁺ VGLUT2⁺ TH⁻), A5-like (PHOX2B⁺; TH⁺; VGLUT2⁻), and C1-like (PHOX2B⁺; TH⁺; VGLUT2⁺) neurons are marked by a filled arrowhead, open arrowhead, and an arrow, respectively.
- (E) Schematic showing MEA analysis of day-60 control HBSOs.
- (F) Firing rate of HBSO neurons in response to different CO₂ levels and RTN blocker (KCNQ channel activator, retigabine). The mean spike firing rate of each MEA recording was normalized with the first recording undertaken in 5% CO₂ condition to calculate the fold change ± SEM from ≥ 9 independent experiments per group. One-way ANOVA.
- (G) UMAP projection of all 23,088 individual cells from day-60 HBSOs, colored by cell types.
- (H) Violin plots showing the key markers of six main cell types. OPC, oligodendrocyte progenitor cell.
- (I) Violin plots showing the key markers of six neuronal subtypes.
- (J) Expression of hindbrain markers (*HOXA2*, *HOXB2*, and *NKX2-2*) in the HBSO cells.
- (K) Relative expression of regional markers *TOX3* (r5) and *PRDX6* (r6) in HCOs and HBSOs.
- (L) Pathway scores of hindbrain development in HCOs and HBSOs. p value (non-parametric Wilcoxon rank-sum test) from comparing HBSOs and HCOs is shown. ****p value < 0.0001. See also Figure S1 and Data S1.

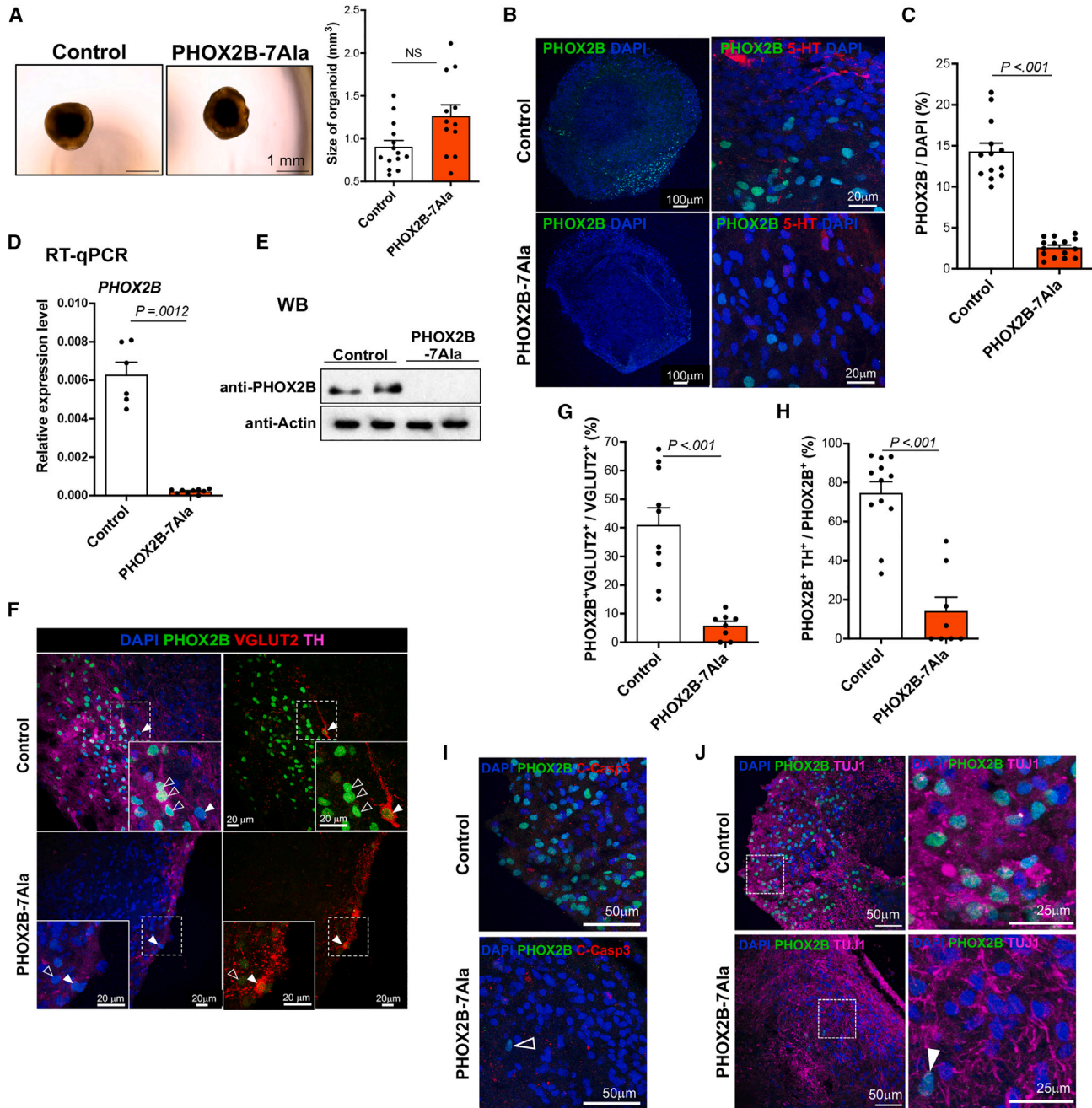


Figure 2. Detrimental effect of PHOX2B-7Ala in the generation of RTN-like neurons in HBSOs

(A) Representative phase-contrast images of the day-60 control and PHOX2B-7Ala HBSOs. Bar chart showing the sizes of the day-60 control and PHOX2B-7Ala HBSOs (mean \pm SEM). $n \geq 9$ per group from three independent experiments. Unpaired t test; NS, non-significant. (B) Immunostaining of PHOX2B, 5-HT in the day-60 control and PHOX2B-7Ala HBSOs. (C) Bar charts showing the percentages of PHOX2B⁺ cells in the day-60 HBSOs derived from the control and PHOX2B-PARM mutants (mean \pm SEM). $n \geq 8$ per group from three independent experiments. (D) qRT-PCR and (E) western blot analyses of PHOX2B expression in the day-60 control and PHOX2B-7Ala HBSOs. Data are represented as mean \pm SEM. $n \geq 9$ per group from three independent experiments. Unpaired t test. (F) Immunostaining of PHOX2B, TH, and VGLUT2 in the day-60 control and PHOX2B-7Ala HBSOs. The inset on the bottom is an enlargement of a square region in the image. Filled and open arrow heads mark the RTN-like (PHOX2B⁺ VGLUT2⁺ TH⁻) and PHOX2B⁺ TH⁺ neurons, respectively.

(legend continued on next page)



from embryonic (La Manno et al., 2021) and adolescent (Zeisel et al., 2018) mouse brains were used as references to annotate the HBSO cells (Figure S1B). 11 main cell types were found in the HBSOs (Figure 1G) with approximately 40% expressing pan-neuronal markers (*NEFL*, *ELAVL2*, *ELAVL4*, and *TUBB3*), 45% expressing glial markers (*EDNRB* and *FABP7*), and the remaining 5% exhibiting molecular signatures resembling radial glia, astrocytes, Schwann cells, or oligodendrocyte progenitor cells (OPCs) (Figure 1H and Data S1).

Using an unsupervised clustering analysis (Liu et al., 2020), HBSO neurons were then classified into four subclasses: cholinergic (*TAC1*⁺, *ACHE*⁺), serotonergic (*GATA2*⁺, *SLC17A8*⁺), GABAergic (*GAD1*⁺, *GAD2*⁺), and glutamatergic (*SLC17A6*⁺, *NRN1*⁺). In addition, there were two distinct groups of *PHOX2B*⁺ neurons with differential expression profiles (*PHOX2B*^{Low} and *PHOX2B*^{High}) (Figures 1I and 1G, Data S1). *PHOX2B*^{Low} group also expressed the glutamatergic marker (*SLC17A6*, which encodes VGLUT2), representing RTN-like neurons, while *PHOX2B*^{High} neurons would be the cholinergic population of *PHOX2B*⁺ hindbrain neurons.

The day-60 HBSOs expressed various caudal hindbrain markers (*HoxA2*, *HoxB2*, and *NKX2-2*) and region-specific markers of r5 (*TOX3*) and r6 (*PRDX6*) (Figures 1J and 1K). Gene Ontology (GO) term enrichment analysis of global gene expression profiles revealed that pathways associated with hindbrain development (GO: 0030902) were highly enriched in the HBSOs in comparison to the HCOs (Figure 1L). In sum, HBSOs exhibited unique hindbrain-specific molecular signatures and comprised the major neuronal subtypes found in the mouse hindbrain/brainstem (La Manno et al., 2021; Liu et al., 2020), including glutamatergic *PHOX2B*⁺ neurons.

PHOX2B-7Ala hampers the generation of hindbrain/RTN neurons as revealed by the HBSO model

Using the newly established HBSO model, we examined the effect of *PHOX2B*-PARMs on the development of RTN neurons, particularly focusing on *PHOX2B*+7Ala PARM, the most common form of PARMs. Using CRISPR-Cas9-mediated homology-directed repair (HDR) platform, seven additional trinucleotide repeats (+7Ala) were introduced into the polyalanine tract of *PHOX2B* (Figure S2). An in-frame insertion of an enhanced green fluorescent protein with a 2A self-cleaving peptide was added immediately after the stop codon of *PHOX2B* to allow subsequent detection of the PARM-expressing mutant cells (Figure S2). At day 60,

the HBSOs generated from *PHOX2B*-7Ala-hPSCs had a comparable size with the control HBSOs (Figure 2A). However, compared with the control, fewer *PHOX2B*⁺ cells were observed, and only a few were found adjacent to 5-HT⁺ neurons in the *PHOX2B*-7Ala HBSOs (Figures 2B and 2C). The loss of *PHOX2B*-expressing cells in *PHOX2B*-7Ala HBSOs was further confirmed by reverse transcription quantitative PCR (qRT-PCR) (Figure 2D) and western blot (Figure 2E) analyses. Consistently, *PHOX2B*⁺ TH⁺ neurons and *PHOX2B*⁺ VGLUT2⁺TH⁻ RTN neurons were barely found in the *PHOX2B*-7Ala HBSOs (Figure 2F). The percentages of *PHOX2B*⁺VGLUT2⁺ (Figure 2G) and *PHOX2B*⁺TH⁺ (Figure 2H) neurons drastically decreased in the *PHOX2B*-7Ala HBSOs. In both the control and *PHOX2B*-7Ala HBSOs, all *PHOX2B*⁺ neurons were negative for apoptotic markers (cleaved caspase-3, C-Casp3⁻) (Figure 2I) and expressed pan-neuronal marker (TUJ1) (Figure 2J), suggesting that the loss of *PHOX2B*⁺ neurons in the mutant HBSOs is unlikely due to the poor survival or neuronal differentiation defect of *PHOX2B*-7Ala-expressing cells.

PHOX2B-7Ala HBSOs exhibit aberrant neuronal differentiation paths and hindbrain signatures

To delineate how *PHOX2B*-7Ala interferes the formation of the respiratory unit, another 11,741 cells from day-60 *PHOX2B*-7Ala HBSOs were sequenced. Despite the presence of the main neuronal and glial cell subtypes in the *PHOX2B*-7Ala HBSOs, an obvious change in the cellular composition of the neuronal population was observed (Figures S3A and S3B). RNA velocity analyses revealed that neuronal differentiation paths for both glutamatergic and GABAergic lineages were disrupted (Figure 3A), accompanied by increased proportions of cholinergic and serotonergic-like cells in the *PHOX2B*-7Ala HBSOs (Figure 3B). In addition, the *PHOX2B*^{High} population was almost completely diminished, and the *PHOX2B*-expressing cells only expressed minimal levels of *PHOX2B* in the *PHOX2B*-7Ala HBSOs (Figure 3B). Thus, the loss of *PHOX2B*⁺ neurons in *PHOX2B*-7Ala HBSOs likely interferes with the pattern and/or development of the hindbrain and respiratory unit. A total of 642 genes (differentially expressed genes, DEGs) were found differentially expressed in *PHOX2B*-7Ala HBSOs. They were enriched in pathways such as “neuron differentiation/migration/fate commitment,” “regionalization,” and “hindbrain development” (Figure 3C). Genes associated with neuronal differentiation (*DLX1*, *DLX2*, *NEUROD1*, and *LHX2*) were

(G and H) Bar charts showing the percentages of (G) *PHOX2B*⁺VGLUT2⁺ and (H) *PHOX2B*⁺TH⁺ cells in the day-60 control and *PHOX2B*-7Ala HBSOs (mean ± SEM). n ≥ 8 per group from three independent experiments. Unpaired t test.

(I and J) Immunostaining of *PHOX2B* with (I) C-Casp3 and (J) TUJ1 (an enlargement of a square is shown in the right panel) in the day-60 control and *PHOX2B*-7Ala HBSOs. Mutant *PHOX2B*⁺ neurons that were viable (C-Casp3⁻) and expressed pan-neuronal marker (TUJ1⁺) are marked by open and filled arrowheads, respectively. See also Figure S2.

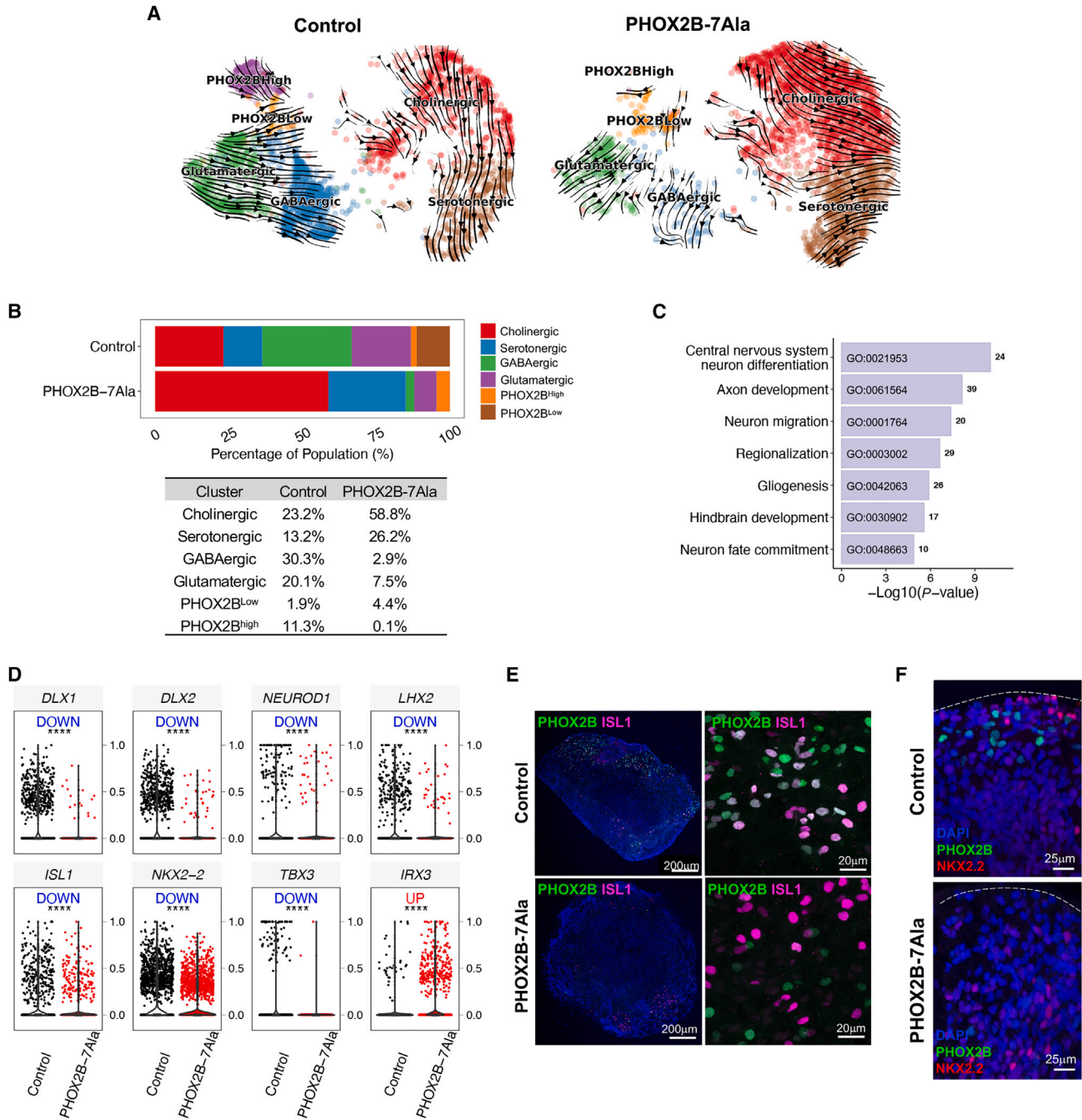


Figure 3. Aberrant differentiation and hindbrain signatures in the PHOX2B-7Ala HBSOs

(A) RNA velocity analyses revealed the differentiation paths of various neuronal subtypes were perturbed in the PHOX2B-7Ala HBSOs. (B) Barplot showing the population size difference of six neuronal subtypes between the control and PHOX2B-7Ala mutant, and the sizes of each population are listed in the bottom table. (C) Barplot showing the disrupted pathways in pooled neuronal cells in PHOX2B-7Ala HBSOs. (D) Violin plots showing the key DEGs involved in neuronal differentiation (upper panel) and hindbrain regionalization (lower panel) in PHOX2B-7Ala mutant. (E and F) Immunostaining of (E) PHOX2B and ISL1 and (F) NKX2-2 in the day-60 control and PHOX2B-7Ala HBSOs. Dotted lines mark the outer surface of the HBSOs. See also [Figure S3](#).



consistently downregulated in PHOX2B-7Ala neurons, and genes implicated in hindbrain morphogenesis (*ISL1*, *NKX2-2*, and *TBX3*) and the midbrain-hindbrain boundary development (*IRX3*) were also dysregulated (Figure 3D). Subsequent immunostaining of the hindbrain marker (*ISL1*) with PHOX2B demonstrated that most PHOX2B⁺ cells in the PHOX2B-7Ala HBSOs did not co-express *ISL1*, suggesting a potential loss of hindbrain identity in the PHOX2B-7Ala-expressing cells (Figure 3E). Consistent with this observation, the NKX2.2⁺ domain (the inferred mantle layer of the hindbrain) shifted from the outer layer in the control HBSOs to the inner layer in the PHOX2B-7Ala HBSOs (Figure 3F), indicating that PHOX2B-7Ala perturbs the patterning of HBSOs.

Depletion of PHOX2B⁺ glutamatergic neurons in the PHOX2B-PARM HCOs

We next sought to address the hindbrain patterning defects associated with the PHOX2B-PARMs unbiasedly using unguided HCOs (Figure S4A). The control unguided HCOs comprised the TBR1⁺ forebrain, FOXA2⁺ midbrain, and *ISL1*⁺ hindbrain regions (Figure 4A). Importantly, PHOX2B⁺ cells were mainly co-localized in the *ISL1*⁺ hindbrain region where the A5, C1 and RTN-like neurons were found near to the 5-HT⁺ neurons (Figure 4B), forming a respiratory center-like region. In parallel, we generated two additional PHOX2B mutant hPSC lines carrying +5Ala- and +13Ala-PARM in PHOX2B for the subsequent comparative studies (Figures 4C and S2). The general morphology, size, and regional diversity of day-60 HCOs derived from all three PHOX2B-PARM hPSC lines were highly comparable to the control (Figures 4D and S4B). Unlike the HBSO model, we detected more cells expressing high levels of PHOX2B in the mutant HCOs. In both the control and mutants, PHOX2B⁺ cells were largely clustered near 5-HT⁺ neurons to form the respiratory center-like regions of comparable sizes (Figure S4C). The A5-like regions were identified in the control and all PHOX2B-PARM HCOs (Figure 4E). However, the C1-like region was absent in the PHOX2B-7Ala and PHOX2B-13Ala HCOs, whereas the PHOX2B-5Ala HCOs contained a slightly lower percentage of RTN-like neurons than the control HCOs in the respiratory center-like regions (Figure 4E). Although the number of PHOX2B-expressing cells was comparable between the control and all the PHOX2B-PARMs mutant HCOs (Figure 4F), the percentages of PHOX2B⁺; VGLUT2⁺ cells were significantly lower in the PHOX2B-7Ala and PHOX2B-13Ala HCOs than in the control HCOs (Figure 4G). These results demonstrated that PHOX2B-PARMs disrupt the formation of PHOX2B⁺; VGLUT2⁺ RTN neurons, as observed in the PHOX2B-7Ala-HBSOs. Moreover, using the HCO model, we demonstrated the direct correlation between the severity of the defect and the length of PARMs on the

formation of PHOX2B⁺ domains during the hindbrain development.

PARM interrupts the progenitor-to-neuron transition of PHOX2B⁺ cells in HCOs

PHOX2B⁺ cells could be found in the PHOX2B-7Ala HCOs, so we then sequenced PHOX2B-7Ala day-60 HCOs at high resolution (Figure S5A). We projected all single cells from the control and PHOX2B-7Ala PARM HCOs on a *t*-distributed stochastic neighbor embedding (*t*-SNE) plot (Figures S5B–S5D) and identified 16 transcriptionally distinct clusters (Data S2). After processing with Seurat software (Hao et al., 2021), the 16 unbiased clusters were further classified into six cell types, including neural stem cells (NSCs), radial glia cells (RGCs), intermediate progenitors (IPs), cortical neurons (CNs), midbrain/hindbrain (M/H), and mesenchymal-like cells (MCs) (Figures 5A, S6A, and S6B and Data S3) based on the expression of canonical markers and cell annotations from a public scRNA-seq dataset of 2-month-old HCOs (Kanton et al., 2019).

Unexpectedly, the expression of *PHOX2B* was extremely low in HCO cells (Figure S7C). This may be due to the high cell heterogeneity in the HCOs, leading to a high dropout rate of rare cells in the 10X Genomics platform (Kim et al., 2020), which makes most of the *PHOX2B* of relatively short transcript length undetectable. Thus, we applied Markov affinity-based graph imputation of cells to denoise the cell count matrix and fill in the missing transcripts (van Dijk et al., 2018). The expression of *PHOX2B* could be recovered well and comparable numbers of *PHOX2B*⁺ cells were identified in the control and PHOX2B-7Ala HCOs (Figure S6D). Most of the *PHOX2B*⁺ cells were found in cell clusters inferred to be less mature progenitors (IPs) or more mature neurons (CNs), and a few were categorized into NSCs (Figures 5B and 5C). We next inferred the lineage relationship among *PHOX2B*⁺ cells in the control HCOs using principal component analysis (PCA). The transition states that linked NSCs through IPs to CNs could be well represented by PC1, while the diversity of CNs was reflected on PC2 (Figure 5D). In the control HCOs, only a small portion of *PHOX2B*⁺ cells remained as NSC/IPs, resided at the beginning of the PC1 axis, and expressed NSC (*SOX2*, *PAX6*, *SOX9*) or IP (*EOMES*) markers, while the majority of *PHOX2B*⁺ cells were found at the end of the PC1 axis with higher expression of mature neuronal markers (*SOX11* and *NEUROD6*), suggesting that most *PHOX2B*⁺ cells were mature neurons (CNs) (Figures 5D and 5E). Although a similar differentiation trajectory (Figures 5F and 5G) was detected in PHOX2B-7Ala HCOs, the percentage of *PHOX2B*⁺ cells in the CN state was significantly reduced, and more *PHOX2B*⁺ cells remained in the progenitor (IP) state in the PHOX2B-7Ala HCOs (Figure 5H). Subsequent immunofluorescence analyses of

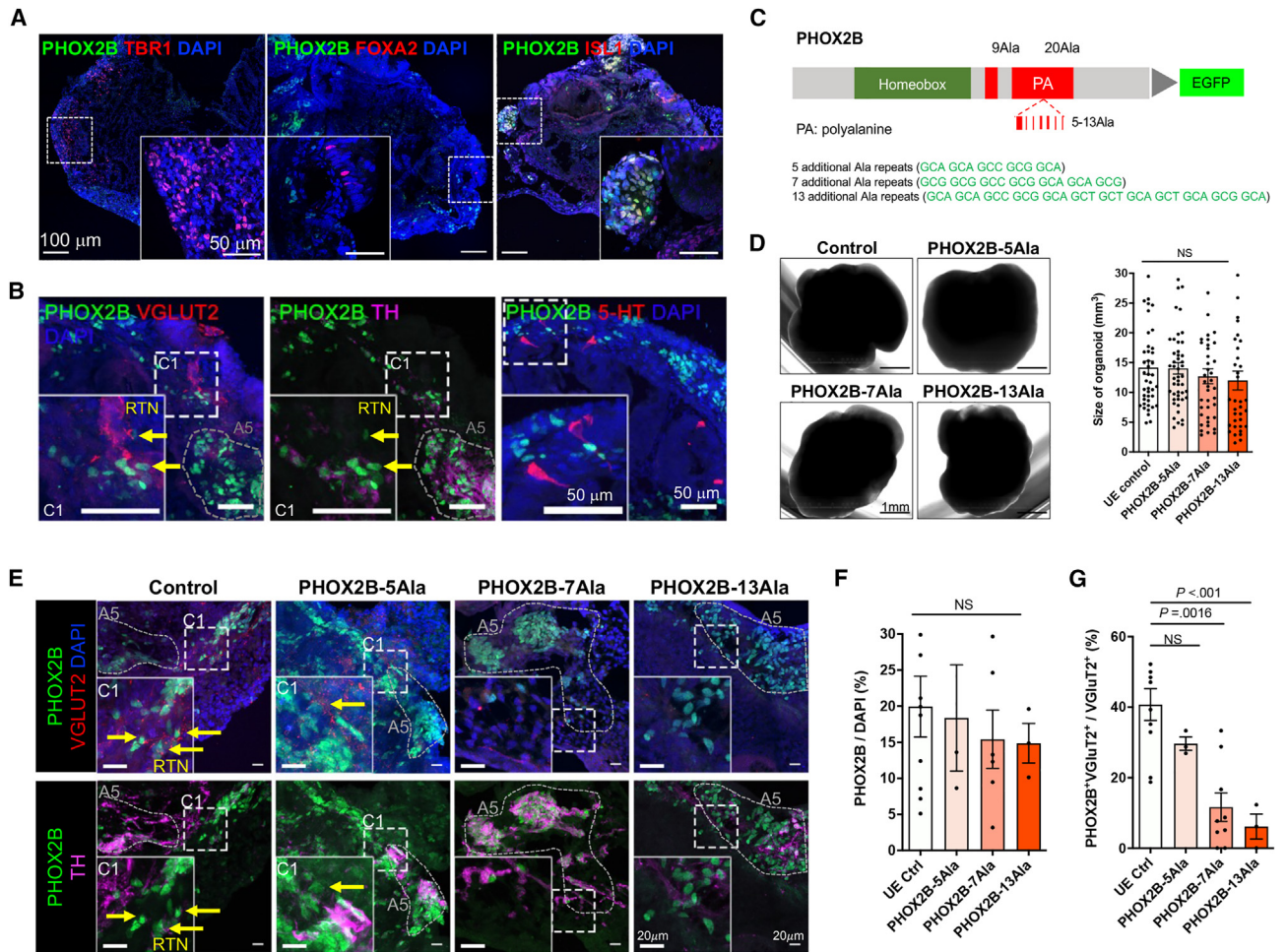


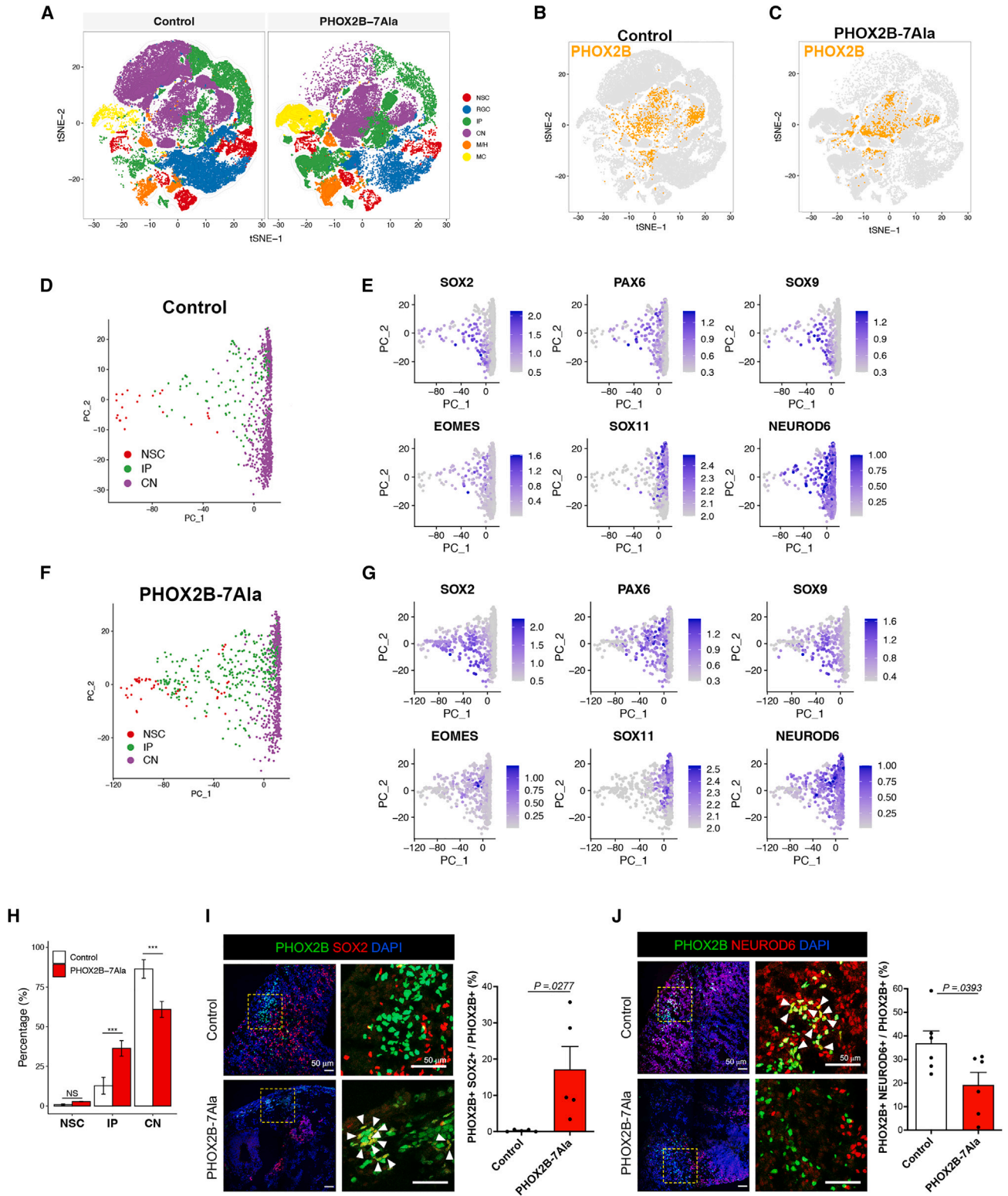
Figure 4. PHOX2B-PARMs disrupt the formation of respiratory center-like region

(A) Immunostaining of PHOX2B and markers of forebrain (TBR1), midbrain (FOXA2), and hindbrain (ISL1) in the day-60 control HCOs. (B) Immunostaining of different markers of the respiratory center-like region in the day-60 control HCOs. Yellow arrows mark the RTN-like (PHOX2B⁺ VGLUT2⁺ TH⁻) neurons. (C) Schematic showing the additional Ala repeats added to the PHOX2B-PARM mutant hPSC lines. (D) Representative phase-contrast images of day-60 HCOs derived from the control and the PHOX2B-PARM mutants. Bar chart showing the sizes of day-60 HCOs derived from the control and the PHOX2B-PARM mutants (mean ± SEM). n ≥ 36 per group from four independent experiments. One-way ANOVA; NS, non-significant. (E) Immunostaining of markers of A5 domain (PHOX2B⁺; TH⁺; VGLUT2⁻), C1 domain (PHOX2B⁺; TH⁺; VGLUT2⁺), and RTN neurons (PHOX2B⁺; TH⁻; VGLUT2⁺) in the day-60 HCOs derived from the control and the PHOX2B-PARM mutants. Yellow arrows mark the RTN-like (PHOX2B⁺ VGLUT2⁺ TH⁻) neurons. (F and G) Bar charts showing the percentages of (F) PHOX2B⁺ and (G) PHOX2B⁺ VGLUT2⁺ double-positive cells in respiratory center-like region of the day-60 HCOs derived from the control and PHOX2B-PARM mutants. n ≥ 3 per group from three independent experiments. One-way ANOVA; NS, non-significant. All the insets on the bottom of the immunostaining image are the enlargement of the respective square regions in the images. See also Figure S4.

day-60 HCOs further confirmed the higher percentage of PHOX2B⁺ cells in the NSC/IP state (PHOX2B⁺; SOX2⁺) (Figure 5I), accompanied by a reduced percentage of mature PHOX2B⁺ neurons (PHOX2B⁺; NEUROD6⁺) (Figure 5J) in the PHOX2B-7Ala HCOs when compared with the control. Thus, PHOX2B-7Ala interrupted the progenitor-to-neuron transition of the PHOX2B⁺ neurons.

Dysregulation of pattern specification pathway genes and loss of PHOX2B⁺ neurons in OTX2⁺ domain of PHOX2B-7Ala HCOs

The mutant PHOX2B proteins were largely localized at the nuclei of the HCO neurons, where the expression of the PHOX2B-7Ala mutant allele was confirmed by the co-expression of GFP signals (Figure 6A). Thus, we performed



(legend on next page)



single-cell regulatory network inference and clustering analysis (Aibar et al., 2017) to establish a gene regulatory network (GRN) of *PHOX2B* in the control and mutant HCOs. *PHOX2B-7Ala* cells showed a different regulatory architecture from that of the control HCOs (Figure 6B). In mice, *Phox2b* upregulates *Phox2a*, *Isl1*, *Tubb3*, and *Ebf1-3* and downregulates *Ascl1* and *Nkx2.2* during the hindbrain development (Pattyn et al., 2000). We observed a similar expression pattern of these genes in the cells expressing *PHOX2B-7Ala* but with the greater changes when compared with the wild-type cells (Figure 6C). Therefore, it is conceivable that *PHOX2B-7Ala* does not simply lead to loss of function or function in a dominant-negative manner but may cause aberrant expression of different gene sets. To address this point, whole-transcriptome correlation analysis was performed to identify *PHOX2B-7Ala*-mediated (activated or repressed) genes and pathways. 2,393 and 640 genes were predicted as *PHOX2B-7Ala* activated (red dots) and repressed (blue dots) genes, respectively, where the activated genes represent the direct targets of *PHOX2B-7Ala* with binding motif(s) in their promoter regions (Figure 6D). Based on the GO database, the putative *PHOX2B-7Ala* activated/repressed genes were mainly implicated in pattern specification or neurogenesis (Figure 6E). Intriguingly, *HOX*- and Hedgehog pathway (*SHH*, *GLI2*)-associated genes belonging to GO: 0007389 (pattern specification process) were found to be significantly upregulated and downregulated, respectively, in the *PHOX2B-7Ala*-expressing cells, suggesting that this pathway was severely interrupted in the mutant cells. The overall changes in these two pathway gene sets in *PHOX2B⁺* and *PHOX2B⁻* cells were then scored using an additive model. The upregulation of *HOX*- and the downregulation of Hedgehog pathway-associated genes implicated in pattern specification were found in all the *PHOX2B⁺* cells expressing both wild-type and mutant forms of *PHOX2B*, but their \log_2 fold changes (*PHOX2B⁺*/*PHOX2B⁻*) were much

higher in the cells expressing mutant *PHOX2B* (Figure 6F), including upregulation of *HOX* genes (Figure 6G) and downregulation of multiple *SHH* downstream effectors (Figure 6H). Noteworthy, the Hedgehog pathway-associated genes were slightly affected in *PHOX2B⁻* cells in the *PHOX2B-7Ala* mutant HCOs (Figure 6F), suggesting that the patterning defects in *PHOX2B⁺* may also influence neighboring *PHOX2B⁻* cells and their development. These analyses suggest that PARMs in *PHOX2B* likely alter its transcriptional activity, leading to either the overactivation or downregulation of its target genes.

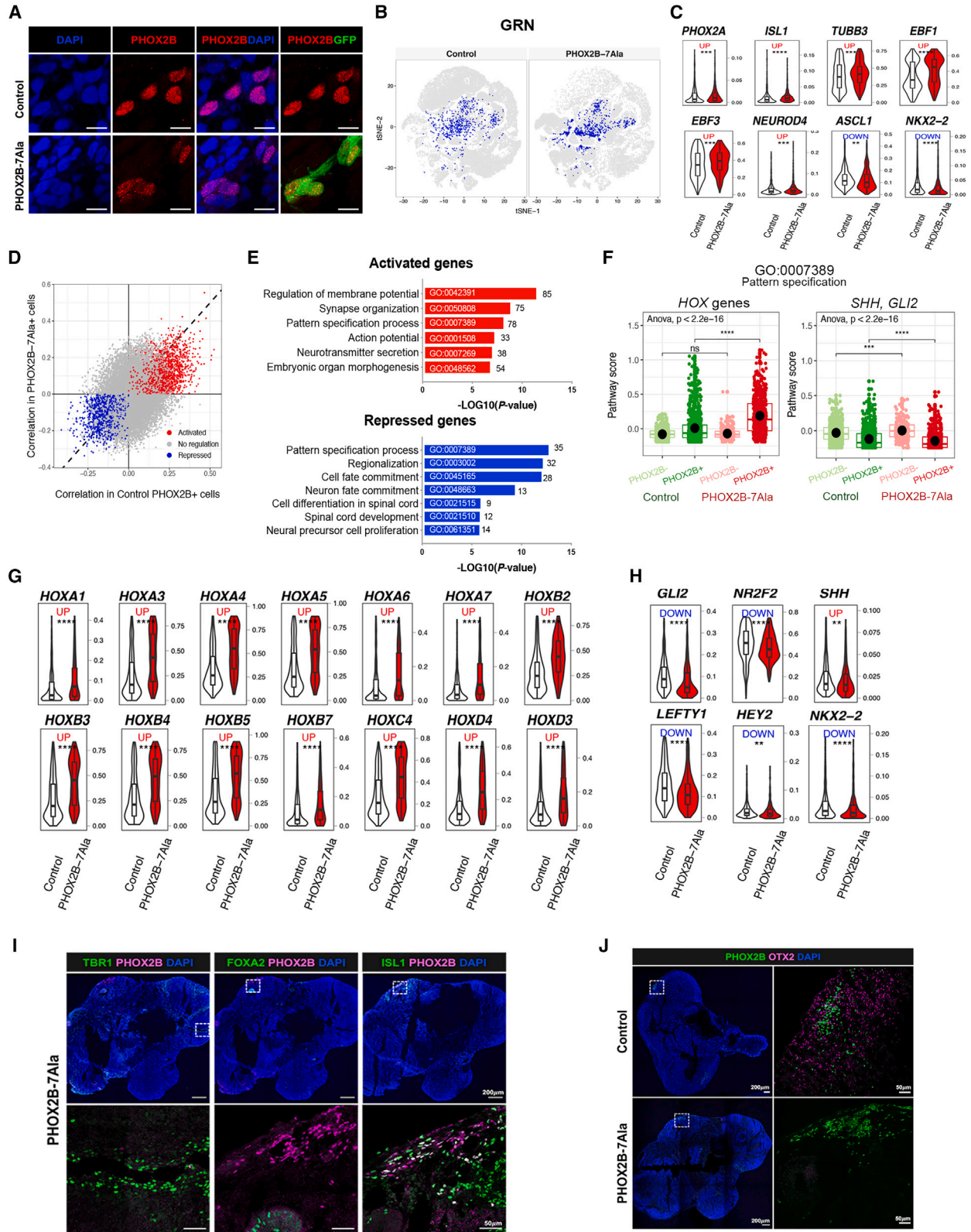
Although some of the mutant *PHOX2B⁺* cells still retained hindbrain identity and were localized largely in the *ISL1⁺* hindbrain region and not in the *FOXA2⁺* midbrain region or the *TBR1⁺* forebrain region of the HCOs (Figure 6I), they might have lost some patterning information. For instance, in control HCOs, some *PHOX2B⁺* cells were found in the *OTX2⁺* domain of the mid-hindbrain boundary (MHB), but this was not observed in mutant HCOs (Figure 6J), implying that the genetic program for the positioning of *PHOX2B⁺* cells may be altered in mutant HCOs. *Phox2b* has been suggested to regulate dopaminergic neuron development in the embryonic mouse midbrain (Hoekstra et al., 2012), so *PHOX2B-7Ala* may also interrupt the formation of dopaminergic neurons in the MHB. Taken together, we found that the pattern specification genes were severely interrupted in the mutant *PHOX2B⁺* cells, with a concomitant loss of *PHOX2B⁺* cells in the respiratory center and *OTX2⁺* domain in the *PHOX2B-7Ala* HCOs.

An HBSO model of CCHS

We next aimed to use the HBSOs to model the CCHS. A patient-specific hPSC line (15C11) was established from skin biopsy of a CCHS patient, who carried a heterozygous +7Ala repeat mutation in the *PHOX2B* (Figures 7A and S7A–S7D). The impact of the +7Ala-PARM was then demonstrated by

Figure 5. scRNA-seq analysis of HCOs reveals that *PHOX2B*-PARM interrupts the progenitor-to-neuronal transition of *PHOX2B⁺* cells

(A) *t*-SNE projection of all 72,800 individual cells from day-60 HCOs into six main cell types, colored by cell types. *PHOX2B⁺* cells in (B) control and (C) *PHOX2B-7Ala* HCOs after imputation analysis.
(D) Trajectory constructed by PCA analysis shows the lineage progression of *PHOX2B⁺* cells from NSC to IP and CN states in the control HCOs.
(E) Canonical markers expressed in *PHOX2B⁺* cells at NSC, IP, and CN states in the control HCOs.
(F) Trajectory constructed by PCA analysis shows the lineage progression of *PHOX2B⁺* cells from NSC to IP and CN states in the *PHOX2B-7Ala* HCOs.
(G) Canonical markers expressed in *PHOX2B⁺* cells at NSC, IP, and CN states in the *PHOX2B-7Ala* HCOs.
(H) Barplot showing the population sizes of *PHOX2B⁺* cells at NSC, IP, and CN states in the control and *PHOX2B-7Ala* HCOs (mean \pm SEM). ***p* < 0.05 and ****p* < 0.001; NS, non-significant.
(I and J) Immunostaining of (I) *PHOX2B⁺*; *SOX2⁺* and (J) *PHOX2B⁺*; *NEUROD6⁺* cells in the control and *PHOX2B-7Ala* mutant HCOs as marked by the arrowheads. An enlargement of a square region in the image is shown in the right panel. Bar charts showing the quantitative data represented as mean \pm SEM. *n* \geq 3 per group from three independent experiments. Unpaired *t* test; two-sided. NSC, neural stem cells; RGC, radial glial cells; IP, intermediate progenitors; CN, cortical neurons; M/H, mid/hindbrain cells; MC, mesenchymal-like cells. See also Figures S5–S7 and Data S2.



(legend on next page)



comparing to the isogenic “corrected” line (15C11-C) where the heterozygous +7Ala repeat mutation in the *PHOX2B* locus was “corrected” using CRISPR-Cas9-mediated HDR (Figures 7B and S2). The 15C11 HBSOs had defects similar to those observed in the PHOX2B-7Ala HBSOs, including the loss of PHOX2B⁺ (Figure 7C), PHOX2B⁺ TH⁺, and PHOX2B⁺ VGLUT2⁺ neurons (Figure 7D). These defects were significantly rescued in the 15C11-C HBSOs (Figures 7E–7G), suggesting that the PHOX2B-associated CCHS phenotypes can be nicely recapitulated by the HBSOs.

DISCUSSION

In this study, we used hPSC-derived regionalized (HBSOs) and unguided (HCOs) brain organoids to study the molecular controls underpinning the formation of the hypercapnia-responsive domain of the respiratory center and the molecular basis of CCHS. We presented a robust differentiation protocol to generate HBSOs that contain a diversity of CNS neurons with hindbrain signatures. The HBSOs comprise the respiratory center-like region and RTN-like neurons of a functional response to hypercapnia. Subsequent analysis of the single-cell transcriptomes of the control HBSOs confirmed the presence of the key populations of neurons and glia and the expression of hindbrain markers, resembling the cellular composition and molecular features of the developing mouse hindbrains. More importantly, our data demonstrated PHOX2B-PARMs not only deterred the formation of glutamatergic RTN neurons but also the differentiation of other lineages of hindbrain neurons, perturbing the cellular composition of HBSOs.

The use of self-patterned HCOs further allowed us to unbiasedly reveal the molecular changes associated with PHOX2B-PARMs. PHOX2B-PARMs not only interfered with the progenitor-to-neuronal transition of PHOX2B⁺ neurons during neuronal differentiation but also with their morphogenesis and pattern specification. In partic-

ular, many *HOX* genes were dysregulated in the PHOX2B-PARM HCOs. Since *HOX* genes regulate the effectors of SHH signaling as well as ASCL1/NGN signaling during rostral-caudal and dorsoventral patterning specification (Gaufo et al., 2000), PHOX2B-PARMs may disrupt hind-brain development by dysregulating SHH signaling. The defective patterning of PHOX2B⁺ neurons may account for their absence in the OTX⁺ domain and RTN-respiratory center in the PHOX2B-PARM-HCOs and/or HBSOs. In addition, SHH is a key factor for the generation of HBSOs, particularly for ventralizing the organoids to enrich hind-brain neurons, so the loss of response to SHH signaling in PHOX2B-PARMs expressing neurons may lead to the depletion of PHOX2B⁺ neurons in mutant HBSOs. Noteworthy, a delayed maturation of the arcuate nucleus was observed in a syndromic CCHS patient (Tomycz et al., 2010), highlighting the possible association between the delayed neuronal maturation and PHOX2B-PARMs in human.

As demonstrated in this study, the complementary uses of HCO and HBSO models will allow us to address a broad range of scientific questions. For instance, the HCOs are generated at a close-to-physiological condition and driven by the self-patterning signals, allowing the study of the interactions among various functional domains as well as genes implicated in the patterning of the brain, while the HBSOs are enriched with hindbrain neurons with high reproducibility, and that makes it most suitable for functional analyses or drug screening. The hypercapnia-responsive neurons in HBSOs can be easily detected not only based on the expression of the molecular markers but also their electroactivities in response to the change in CO₂ levels, ion channel mediators, or neurotransmitters. This greatly expedites its potential applications for the high-throughput drug screenings.

PHOX2B-PARM proteins, when expressed at a normal endogenous level, still localized in the nuclei of mutant neurons. Our data suggest that PHOX2B-PARMs may

Figure 6. PHOX2B-PARM interrupts the pattern specification of PHOX2B⁺ neurons in HCOs

- (A) Immunostaining showing the nuclear localization of PHOX2B proteins in the day-60 control and PHOX2B-7Ala mutant HCOs.
(B) GRN activity of PHOX2B in the control and mutant HCOs.
(C) Violin plots showing the expression of PHOX2B hindbrain targets in the control and mutant CNs. **p < 0.05, ***p < 0.001, and ****p < 0.0001.
(D) Scatterplot showing the putative PHOX2B-7Ala activated (red) and repressed (blue) targeted genes.
(E) Gene Ontology (GO) enrichment analyses of PHOX2B activated and repressed targeted genes.
(F) Overall pathway scores of embryonic organ morphogenesis and pattern specification. ***p < 0.001 and ****p < 0.0001; ns, non-significant.
(G) Violin plots showing the expression of *HOX* genes in the control and mutant CNs. ****p < 0.0001.
(H) Violin plots showing the expression of Hedgehog pathway genes in the control and mutant CNs. **p < 0.05 and ****p < 0.0001.
(I) Immunostaining of PHOX2B and markers of forebrain, midbrain, and hindbrain (TBR1, FOXA2, and ISL1) in the day-60 PHOX2B-7Ala HCOs.
(J) Immunostaining of PHOX2B and OTX2 in the day-60 control and PHOX2B-7Ala HCOs. An enlargement of a square region in the image is shown in the (I) bottom and (J) right panel.

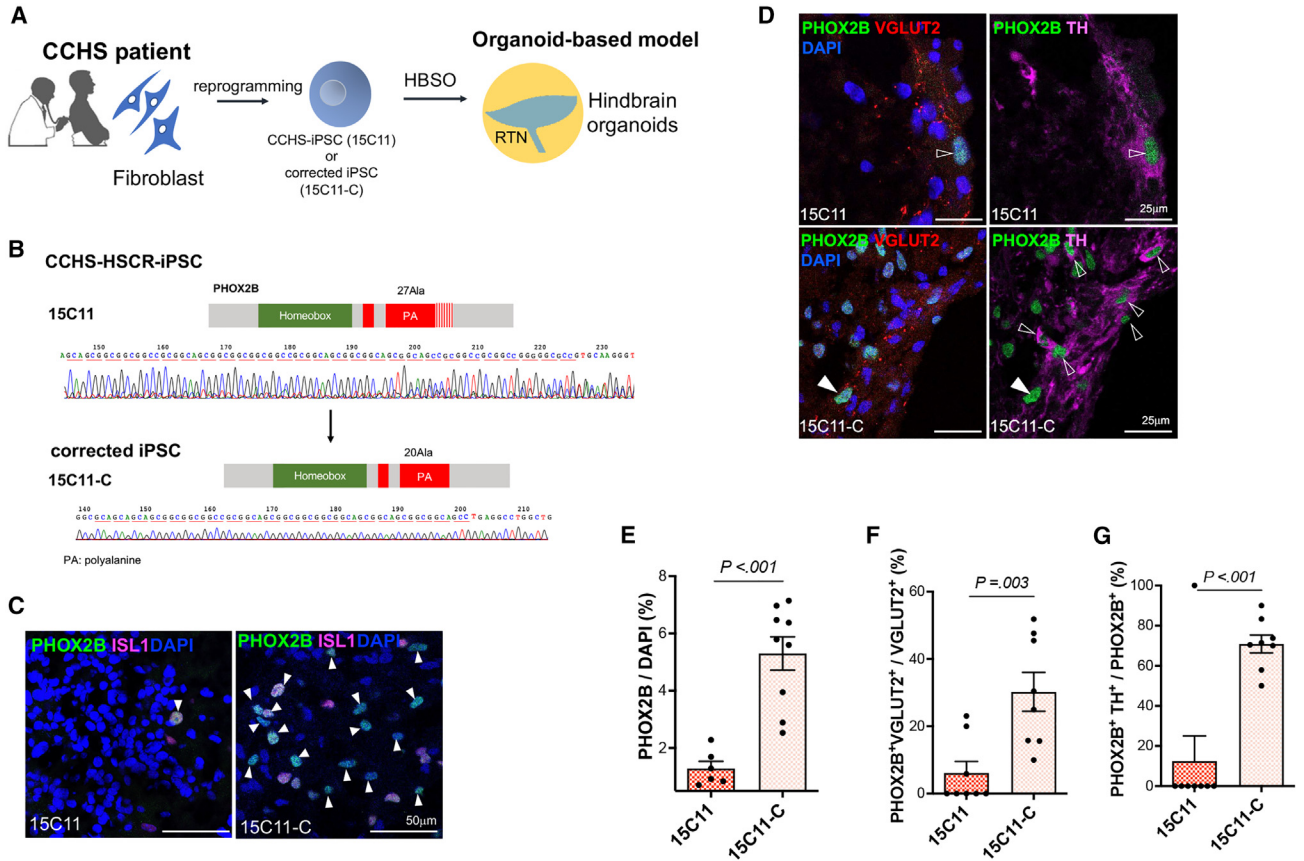


Figure 7. A HBSO model of CCHS

(A) Schematic showing the establishment of hPSC-based model of CCHS. (B) Electrographs of Sanger sequencing of *PHOX2B* exon 3 showing the “correction” of +7Ala-PARM in *PHOX2B* locus. (C) Immunostaining of PHOX2B and ISL1 in the day-60 15C11 and 15C11-C HBSOs. Arrowheads mark the PHOX2B⁺ISL1⁺ neurons. (D) Immunostaining of PHOX2B, TH, and VGLUT2 in the day-60 15C11 and 15C11-C HBSOs. The putative RTN (PHOX2B⁺VGLUT2⁺TH⁻) and PHOX2B⁺TH⁺ neurons are marked by filled and open arrowheads, respectively. (E–G) Bar charts showing the percentages of (E) PHOX2B⁺, (F) PHOX2B⁺VGLUT2⁺, and (G) PHOX2B⁺TH⁺ cells in the day-60 15C11 and 15C11-C HBSOs. Data are represented as mean ± SEM. n ≥ 6 per group from three independent experiments. Unpaired t test, two-sided. See also Figure S7.

have a toxic gain of function that alters their GRNs. Regardless of the length, PHOX2B-PARMs disrupted the formation of glutamatergic RTN neurons, while PARMs with longer alanine repeats also perturbed the formation of PHOX2B⁺VGLUT2⁺TH⁺ neurons in C1. The C1 neurons innervating the A5 domain are important for sympathetic and respiratory outputs (Malheiros-Lima et al., 2022); therefore, the additional loss of C1 neurons associated with the longer polyalanine repetition in PARMs probably leads to more severe breathing defects. Additional proof-of-concept study using a CCHS patient-specific and the “corrected” isogenic hPSC lines further suggests the potential application of HBSOs for disease modeling. Using the experimental paradigm established in this study, HBSOs derived from multiple patient lines can be used in

conjunction with the scRNA-seq platform to further delineate the molecular mechanisms underlying PHOX2B-PARMs in CCHS pathogenesis. In addition, CCHS patients are frequently complicated with Hirschsprung disease (absence of enteric neurons in the distal colon) (Bachetti and Ceccherini, 2020). Therefore, HBSOs and enteric neurons can be derived from the same hPSC lines with identical genetic backgrounds and used for a side-by-side comparison to unveil the causal link between these closely related diseases in the future. In sum, HBSOs and HCOs comprise enriched hindbrain neurons and self-assembled multicomponent structures, respectively, and complementary uses of these two models allow us to unambiguously reveal the detrimental effects of PHOX2B-PARMs in hindbrain development.



EXPERIMENTAL PROCEDURES

Resource availability

Corresponding author

Further information and requests for resources and reagents should be directed to and will be fulfilled by the corresponding author, Elly Ngan (engan@hku.hk).

Materials availability

All unique/stable reagents generated in this study are available from the corresponding author without restriction.

Data and code availability

Raw sequencing data are available in the Sequence Read Archive at the NCBI Center with the accession number PRJNA891126. The processed scRNA-seq datasets are available at <https://doi.org/10.5281/zenodo.7215153>.

The detailed protocols are available in [supplemental experimental procedures](#).

Generation and maintenance of hPSC lines

UE02302 hPSC line was used as the control (Xue et al., 2013). To generate PHOX2B-PARM mutant hPSC line, UE02302 hPSCs were transfected with the mutant *PHOX2B-PARM* donor plasmids together with gRNA constructs targeting *PHOX2B* and a Cas9 nickase expression plasmid by Nucleofection (Lonza). The transfected cells were selected with 0.2 µg/mL puromycin, and the PARM insertions were confirmed with Sanger sequencing. The patient hPSC line (15C11) was generated from skin fibroblast of a CCHS-HSCR patient (Figure S7) with episomal reprogramming vectors as described previously (Lai et al., 2017; Takahashi et al., 2007). The CRISPR-Cas9 homologous recombination strategy was used for the correction of PHOX2B-7Ala mutation in the patient hPSC line with a wild-type *PHOX2B* donor plasmid (15C11-C) ([supplemental experimental procedures](#)). All the hPSC lines were tested *Mycoplasma*-free and maintained in Matrigel-coated plates with mTeSR1 medium.

Generation of HSBOs and HCOs from hPSCs

To generate HSBOs, 2.7×10^6 hPSCs were seeded per well in an AggreWell800 24-well plate with mTeSR1 containing 10 µM Y-27632. 1 day later, the spheroids were transferred to an ultra-low-attachment plate and cultured with Neural Induction Medium. From days 3–6, the organoids were incubated in Neural Differentiation Medium (NDM) with 1 µM LDN-193189, 10 µM SB431542, and 1 µM SAG and kept rotating from day 3 onward. From days 6–12, the organoids were maintained in NDM with 1 µM SAG, 3 µM CHIR99021, and 1 µM RA, and the medium was changed every 2–3 days. From day 12 onward, the organoids were maintained in Neural Maturation Medium with 20 ng/mL BDNF, 20 ng/mL GDNF, 50 nM dibutyryl-cAMP, and 200 µM ascorbic acid. The medium was changed every 3–4 days.

HCOs were generated from hPSCs using a commercially optimized kit, STEMdiff Cerebral Organoid Kit (STEMCELL Technologies), following the manufacturer's protocol.

Details of the cell culture reagents are listed in [supplemental experimental procedures](#) and Table S1.

Multielectrode array analysis

Day 60 HSBOs were dissociated with Papain Dissociation System and seeded into a 24-well CytoView MEA plate pre-coated with 0.1% polyethylenimine and maintained for 2 weeks before MEA analysis. The electric signals were measured at 37°C with 5%–8% CO₂ using Maestro Edge MEA System (Axion Biosystems) in absence or presence of retigabine (10 µM). The recordings were analyzed using AxIS Navigator 1.5 and Neural Metric Tool software.

Reverse transcription quantitative PCR

Total RNA from the organoids were extracted and reverse-transcribed to cDNA. The cDNA samples were amplified with specific primers (Table S2). Each individual sample was assayed in triplicate and normalized with *GAPDH* expression.

Western blot

Protein lysates from HSBOs were separated by SDS-PAGE and then transferred to PVDF membrane. After blocking, the membrane was incubated with primary antibodies, followed by HRP-conjugated secondary antibodies (Table S3). The HRP signals were detected using WesternBright ECL kit.

Immunostaining

Organoids samples were fixed with 4% paraformaldehyde, dehydrated, and embedded in O.C.T. Compound. After blocking, the frozen sections (10–20 µm) were incubated with primary antibodies, followed by the respective secondary antibodies (Table S3).

Droplet-based single-cell RNA-sequencing

Day-60 HSBOs and HCOs were dissociated into single-cell suspension. Viable cells negative for 7-AAD were sorted with BD FACSAria III Cell Sorter and then subjected to 10X Genomics' scRNA-seq with Illumina NextSeq 500. The details of data analyses are available in the [supplemental experimental procedures](#).

Image analysis and statistical analysis

All the fluorescence images were acquired by Carl Zeiss LSM800 or LSM900. Cell numbers were quantified using Fiji ImageJ software (Schindelin et al., 2012; Schneider et al., 2012). Statistical analysis was performed with the software Prism 9.0 (GraphPad). Unless otherwise noted, the data were expressed as mean ± SEM from at least three independent experiments. Two-tailed unpaired Student's t test was used for two-group comparisons. One-way ANOVA, followed by Turkey's multiple comparison test, was used for comparisons involving more than two groups. Probability values $p < 0.05$ were considered statistically significant.

SUPPLEMENTAL INFORMATION

Supplemental information can be found online at <https://doi.org/10.1016/j.stemcr.2023.05.020>.

AUTHOR CONTRIBUTIONS

K.N.C.L., S.T.L., and F.P.L.L. established hPSC lines and performed *in vitro* functional assays. Z.L. performed the bioinformatics



analyses. K.N.C.L., Z.L., and E.S.W.N. prepared the manuscript. E.S.W.N. supervised the project.

ACKNOWLEDGMENTS

The authors acknowledge the assistance of Center of PanorOmic Science (CPOS), Li Ka Shing Faculty of Medicine, The University of Hong Kong. The work described in this paper was substantially supported by the HMRF grants (Project nos. 06173306, 07181926, 08192786) from the Health Department, China Hong Kong and the General Research Fund (GRF: HKU 17108019, 17101320) from the Research Grant Council of Hong Kong Special Administrative Region, China Hong Kong. The study was approved by the Institutional Review Board of The University of Hong Kong and the Hospital Authority (UW 13–419).

CONFLICT OF INTERESTS

The authors are filing a patent related to the method of generating HBSOs as described in this manuscript.

Received: March 29, 2023

Revised: May 24, 2023

Accepted: May 24, 2023

Published: June 22, 2023

REFERENCES

Aibar, S., Gonzalez-Blas, C.B., Moerman, T., Huynh-Thu, V.A., Imrichova, H., Hulselmans, G., Rambow, F., Marine, J.C., Geurts, P., Aerts, J., et al. (2017). SCENIC: single-cell regulatory network inference and clustering. *Nat. Methods* *14*, 1083–1086. <https://doi.org/10.1038/nmeth.4463>.

Amiel, J., Laudier, B., Attie-Bitach, T., Trang, H., de Pontual, L., Gener, B., Trochet, D., Etchevers, H., Ray, P., Simonneau, M., et al. (2003). Polyalanine expansion and frameshift mutations of the paired-like homeobox gene PHOX2B in congenital central hypoventilation syndrome. *Nat. Genet.* *33*, 459–461. <https://doi.org/10.1038/ng1130>.

Bachetti, T., and Ceccherini, I. (2020). Causative and common PHOX2B variants define a broad phenotypic spectrum. *Clin. Genet.* *97*, 103–113. <https://doi.org/10.1111/cge.13633>.

Butts, J.C., Iyer, N., White, N., Thompson, R., Sakiyama-Elbert, S., and McDevitt, T.C. (2019). V2a interneuron differentiation from mouse and human pluripotent stem cells. *Nat. Protoc.* *14*, 3033–3058. <https://doi.org/10.1038/s41596-019-0203-1>.

Dubreuil, V., Ramanantsoa, N., Trochet, D., Vaubourg, V., Amiel, J., Gallego, J., Brunet, J.F., and Goridis, C. (2008). A human mutation in Phox2b causes lack of CO₂ chemosensitivity, fatal central apnea, and specific loss of parafacial neurons. *Proc. Natl. Acad. Sci. USA* *105*, 1067–1072. <https://doi.org/10.1073/pnas.0709115105>.

Dubreuil, V., Thoby-Brisson, M., Rallu, M., Persson, K., Pattyn, A., Birchmeier, C., Brunet, J.F., Fortin, G., and Goridis, C. (2009). Defective respiratory rhythmogenesis and loss of central chemosensitivity in Phox2b mutants targeting retrotrapezoid nucleus neurons. *J. Neurosci.* *29*, 14836–14846. <https://doi.org/10.1523/JNEUROSCI.2623-09.2009>.

Eura, N., Matsui, T.K., Luginbühl, J., Matsubayashi, M., Nanaura, H., Shiota, T., Kinugawa, K., Iguchi, N., Kiriya, T., Zheng, C., et al. (2020). Brainstem organoids from human pluripotent stem cells. *Front. Neurosci.* *14*, 538. <https://doi.org/10.3389/fnins.2020.00538>.

Gaufo, G.O., Flodby, P., and Capecchi, M.R. (2000). Hoxb1 controls effectors of sonic hedgehog and Mash1 signaling pathways. *Development* *127*, 5343–5354. <https://doi.org/10.1242/dev.127.24.5343>.

Giandomenico, S.L., Sutcliffe, M., and Lancaster, M.A. (2021). Generation and long-term culture of advanced cerebral organoids for studying later stages of neural development. *Nat. Protoc.* *16*, 579–602. <https://doi.org/10.1038/s41596-020-00433-w>.

Goridis, C., Dubreuil, V., Thoby-Brisson, M., Fortin, G., and Brunet, J.F. (2010). Phox2b, congenital central hypoventilation syndrome and the control of respiration. *Semin. Cell Dev. Biol.* *21*, 814–822. <https://doi.org/10.1016/j.semcdb.2010.07.006>.

Guyenet, P.G., Mulkey, D.K., Stornetta, R.L., and Bayliss, D.A. (2005). Regulation of ventral surface chemoreceptors by the central respiratory pattern generator. *J. Neurosci.* *25*, 8938–8947. <https://doi.org/10.1523/JNEUROSCI.2415-05.2005>.

Guyenet, P.G., Stornetta, R.L., Souza, G.M.P.R., Abbott, S.B.G., Shi, Y., and Bayliss, D.A. (2019). The retrotrapezoid nucleus: central chemoreceptor and regulator of breathing automaticity. *Trends Neurosci.* *42*, 807–824. <https://doi.org/10.1016/j.tins.2019.09.002>.

Hao, Y., Hao, S., Andersen-Nissen, E., Mauck, W.M., 3rd, Zheng, S., Butler, A., Lee, M.J., Wilk, A.J., Darby, C., Zager, M., et al. (2021). Integrated analysis of multimodal single-cell data. *Cell* *184*, 3573–3587.e29. <https://doi.org/10.1016/j.cell.2021.04.048>.

Hawryluk, J.M., Moreira, T.S., Takakura, A.C., Wenker, I.C., Tzingounis, A.V., and Mulkey, D.K. (2012). KCNQ channels determine serotonergic modulation of ventral surface chemoreceptors and respiratory drive. *J. Neurosci.* *32*, 16943–16952. <https://doi.org/10.1523/JNEUROSCI.3043-12.2012>.

Hoekstra, E.J., Von Oerthel, L., Van Der Linden, A.J.A., and Smidt, M.P. (2012). Phox2b influences the development of a caudal dopaminergic subset. *PLoS One* *7*, e52118. <https://doi.org/10.1371/journal.pone.0052118>.

Kanton, S., Boyle, M.J., He, Z., Santel, M., Weigert, A., Sanchis-Callaja, F., Guijarro, P., Sidow, L., Fleck, J.S., Han, D., et al. (2019). Organoid single-cell genomic atlas uncovers human-specific features of brain development. *Nature* *574*, 418–422. <https://doi.org/10.1038/s41586-019-1654-9>.

Kim, T.H., Zhou, X., and Chen, M. (2020). Demystifying "drop-outs" in single-cell UMI data. *Genome Biol.* *21*, 196. <https://doi.org/10.1186/s13059-020-02096-y>.

La Manno, G., Siletti, K., Furlan, A., Gyllborg, D., Vinsland, E., Mossi Albiach, A., Mattsson Langseth, C., Khven, I., Lederer, A.R., Dratva, L.M., et al. (2021). Molecular architecture of the developing mouse brain. *Nature* *596*, 92–96. <https://doi.org/10.1038/s41586-021-03775-x>.

Lai, F.P.L., Lau, S.T., Wong, J.K.L., Gui, H., Wang, R.X., Zhou, T., Lai, W.H., Tse, H.F., Tam, P.K.H., Garcia-Barcelo, M.M., and Ngan, E.S.W. (2017). Correction of hirschsprung-associated mutations in human induced pluripotent stem cells via clustered regularly interspaced short palindromic repeats/Cas9, restores neural crest cell



- function. *Gastroenterology* 153, 139–153.e8. <https://doi.org/10.1053/j.gastro.2017.03.014>.
- Lancaster, M.A., and Knoblich, J.A. (2014). Generation of cerebral organoids from human pluripotent stem cells. *Nat. Protoc.* 9, 2329–2340. <https://doi.org/10.1038/nprot.2014.158>.
- Lancaster, M.A., Renner, M., Martin, C.A., Wenzel, D., Bicknell, L.S., Hurles, M.E., Homfray, T., Penninger, J.M., Jackson, A.P., and Knoblich, J.A. (2013). Cerebral organoids model human brain development and microcephaly. *Nature* 501, 373–379. <https://doi.org/10.1038/nature12517>.
- Liu, W., Venugopal, S., Majid, S., Ahn, I.S., Diamante, G., Hong, J., Yang, X., and Chandler, S.H. (2020). Single-cell RNA-seq analysis of the brainstem of mutant SOD1 mice reveals perturbed cell types and pathways of amyotrophic lateral sclerosis. *Neurobiol. Dis.* 141, 104877. <https://doi.org/10.1016/j.nbd.2020.104877>.
- Malheiros-Lima, M.R., Silva, T.M., Takakura, A.C., and Moreira, T.S. (2022). A5 noradrenergic-projecting C1 neurons activate sympathetic and breathing outputs in anaesthetized rats. *Exp. Physiol.* 107, 147–160. <https://doi.org/10.1113/EP089691>.
- Matera, I., Bachetti, T., Puppo, F., Di Duca, M., Morandi, F., Casiraghi, G.M., Cilio, M.R., Hennekam, R., Hofstra, R., Schöber, J.G., et al. (2004). PHOX2B mutations and polyalanine expansions correlate with the severity of the respiratory phenotype and associated symptoms in both congenital and late onset Central Hypoventilation syndrome. *J. Med. Genet.* 41, 373–380. <https://doi.org/10.1136/jmg.2003.015412>.
- Moreira, T.S., Takakura, A.C., Czeisler, C., and Otero, J.J. (2016). Respiratory and autonomic dysfunction in congenital central hypoventilation syndrome. *J. Neurophysiol.* 116, 742–752. <https://doi.org/10.1152/jn.00026.2016>.
- Pattyn, A., Hirsch, M., Goridis, C., and Brunet, J.F. (2000). Control of hindbrain motor neuron differentiation by the homeobox gene Phox2b. *Development* 127, 1349–1358. <https://doi.org/10.1242/dev.127.7.1349>.
- Schindelin, J., Arganda-Carreras, I., Frise, E., Kaynig, V., Longair, M., Pietzsch, T., Preibisch, S., Rueden, C., Saalfeld, S., Schmid, B., et al. (2012). Fiji: an open-source platform for biological-image analysis. *Nat. Methods* 9, 676–682. <https://doi.org/10.1038/nmeth.2019>.
- Schneider, C.A., Rasband, W.S., and Eliceiri, K.W. (2012). NIH Image to ImageJ: 25 years of image analysis. *Nat. Methods* 9, 671–675. <https://doi.org/10.1038/nmeth.2089>.
- Takahashi, K., Okita, K., Nakagawa, M., and Yamanaka, S. (2007). Induction of pluripotent stem cells from fibroblast cultures. *Nat. Protoc.* 2, 3081–3089. <https://doi.org/10.1038/nprot.2007.418>.
- Tomycz, N.D., Haynes, R.L., Schmidt, E.F., Ackerson, K., and Kinney, H.C. (2010). Novel neuropathologic findings in the Haddad syndrome. *Acta Neuropathol.* 119, 261–269. <https://doi.org/10.1007/s00401-009-0599-8>.
- van Dijk, D., Sharma, R., Nainys, J., Yim, K., Kathail, P., Carr, A.J., Burdziak, C., Moon, K.R., Chaffer, C.L., Pattabiraman, D., et al. (2018). Recovering gene interactions from single-cell data using data diffusion. *Cell* 174, 716–729.e27. <https://doi.org/10.1016/j.cell.2018.05.061>.
- Xue, Y., Cai, X., Wang, L., Liao, B., Zhang, H., Shan, Y., Chen, Q., Zhou, T., Li, X., Hou, J., et al. (2013). Generating a non-integrating human induced pluripotent stem cell bank from urine-derived cells. *PLoS One* 8, e70573. <https://doi.org/10.1371/journal.pone.0070573>.
- Zeisel, A., Hochgerner, H., Lönnerberg, P., Johnsson, A., Memic, F., van der Zwan, J., Häring, M., Braun, E., Borm, L.E., La Manno, G., et al. (2018). Molecular architecture of the mouse nervous system. *Cell* 174, 999–1014.e22. <https://doi.org/10.1016/j.cell.2018.06.021>.

Stem Cell Reports, Volume 18

Supplemental Information

Organoid models of breathing disorders reveal patterning defect of hindbrain neurons caused by PHOX2B-PARMs

Kathy Nga-Chu Lui, Zhixin Li, Frank Pui-Ling Lai, Sin-Ting Lau, and Elly Sau-Wai Ngan

Description of Supplementary Files

Supplementary Data 1: Markers for 11 clusters in control HBSOs.

Supplementary Data 2: Markers of the 16 clusters identified in control and PHOX2B-7Ala HCOs.

Supplementary Data 3: Markers of the 6 cell types identified in HCOs.

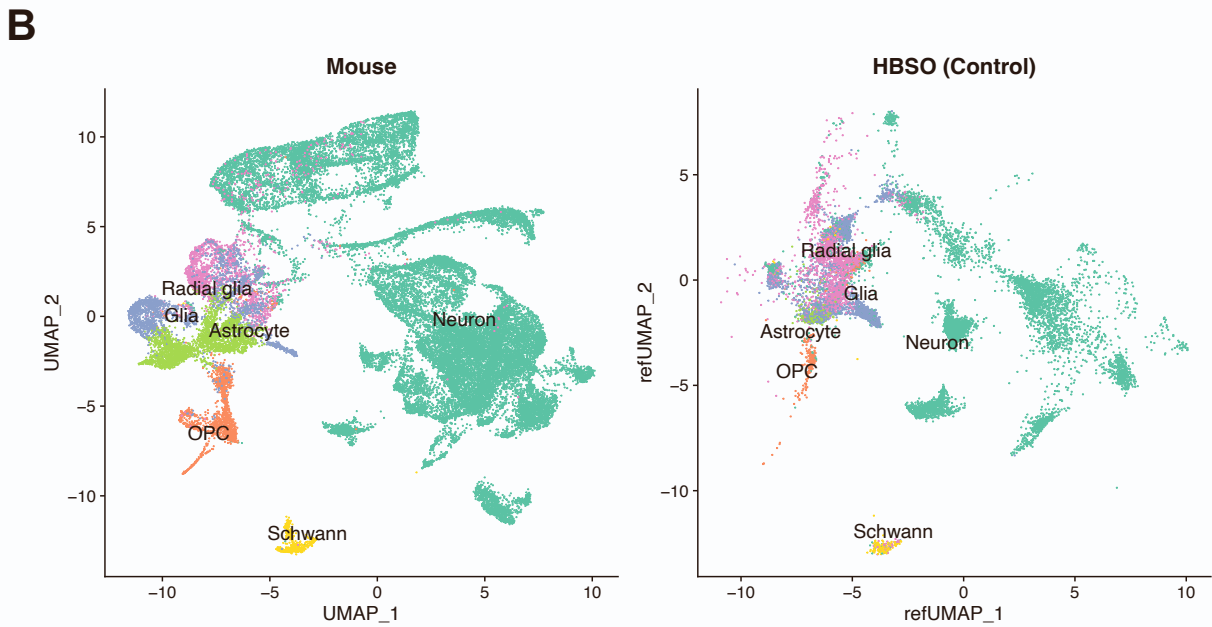
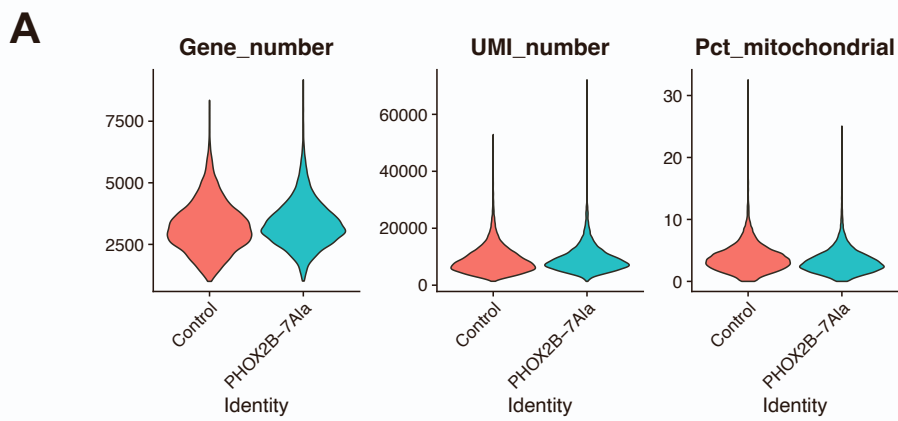
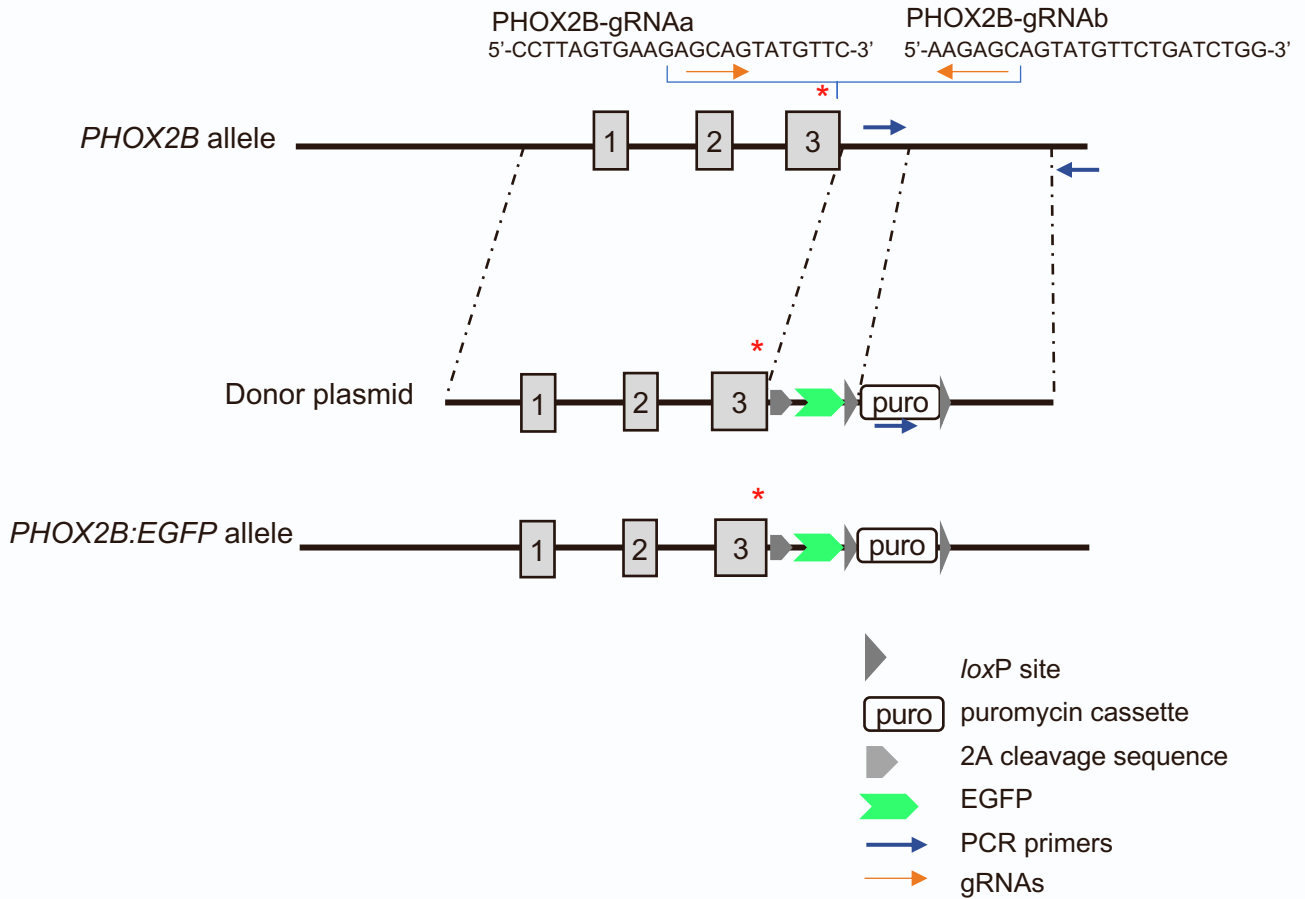


Fig. S1 Quality control and reference-based annotation of HBSO cells. (A) The number of detected gene and UMI number, and percentage of mitochondrial genes between control and PHOX2B-7Ala mutant HBSOs. (B) Distribution of the six main cell types of *in vivo* mouse hindbrain cells from E12-E16 (Manno *et al.*, 2021) and our pooled HBSOs in UMAP plot (colored by cell types). Cell labels were transferred from *in vivo* mouse hindbrain to HBSOs by Seurat.



- * 5 additional Ala repeats (GCA GCA GCC GCG GCA)
 7 additional Ala repeats (GCG GCG GCC GCG GCA GCA GCG)
 13 additional Ala repeats (GCA GCA GCC GCG GCA GCT GCT GCT GCA GCT GCA GCG GCA)

Fig. S2 Targeting strategy for introduction and correction of PARM-mutations in human *PHOX2B* allele. Additional Ala repeats were introduced to the 20-Ala polyalanine tract in exon 3 of *PHOX2B* in the control hPSC line to generate *PHOX2B*-PARM mutant lines by CRISPR-Cas9. The same site in the CCHS-HSCR patient hPSC line (i.e. 15C11) was corrected back to 20-Ala polyalanine tract to generate corrected hPSC line (i.e. 15C11-C).

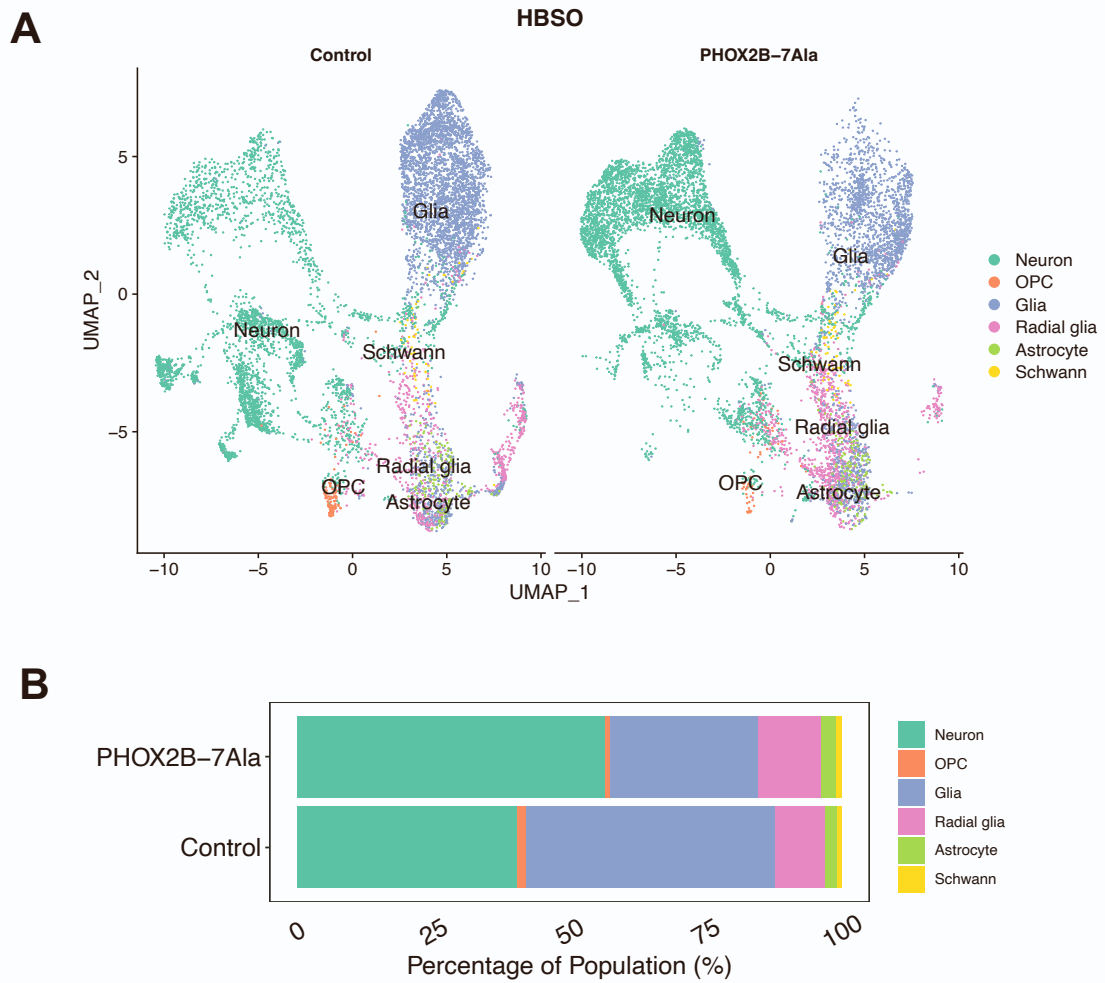


Fig. S3 Cell composition in the control and PHOX2B-7Ala mutant HBSOs as revealed by scRNA-seq. (A) Distribution of the six main cell types of our control and PHOX2B-7Ala mutant HBSOs in a new UMAP plot (colored by cell types). (B) Barplot showing the population size difference of the six main cell types between the control and PHOX2B-7Ala mutant. OPC, oligodendrocyte progenitor cell.

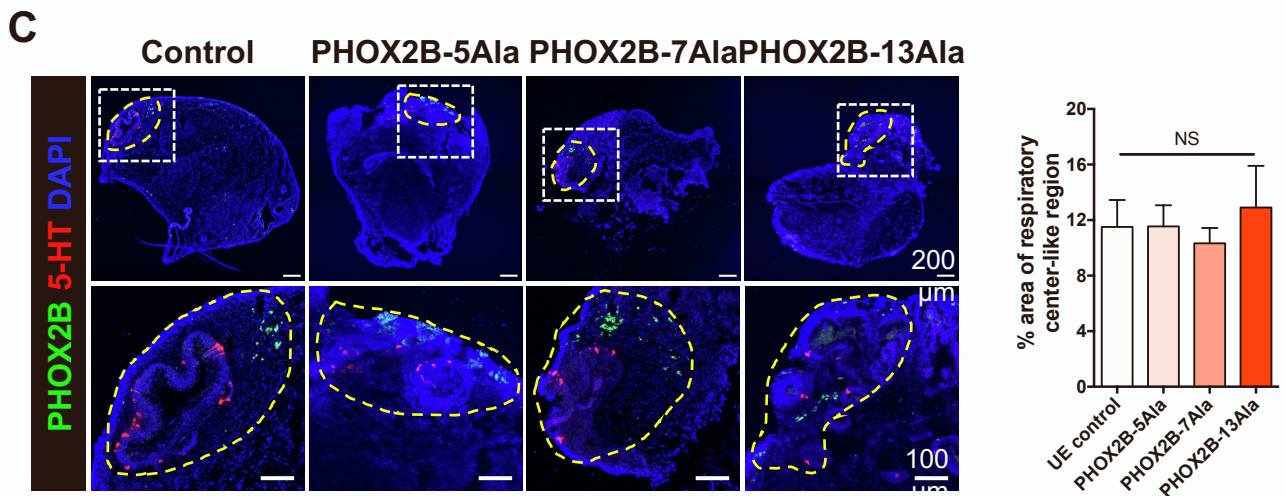
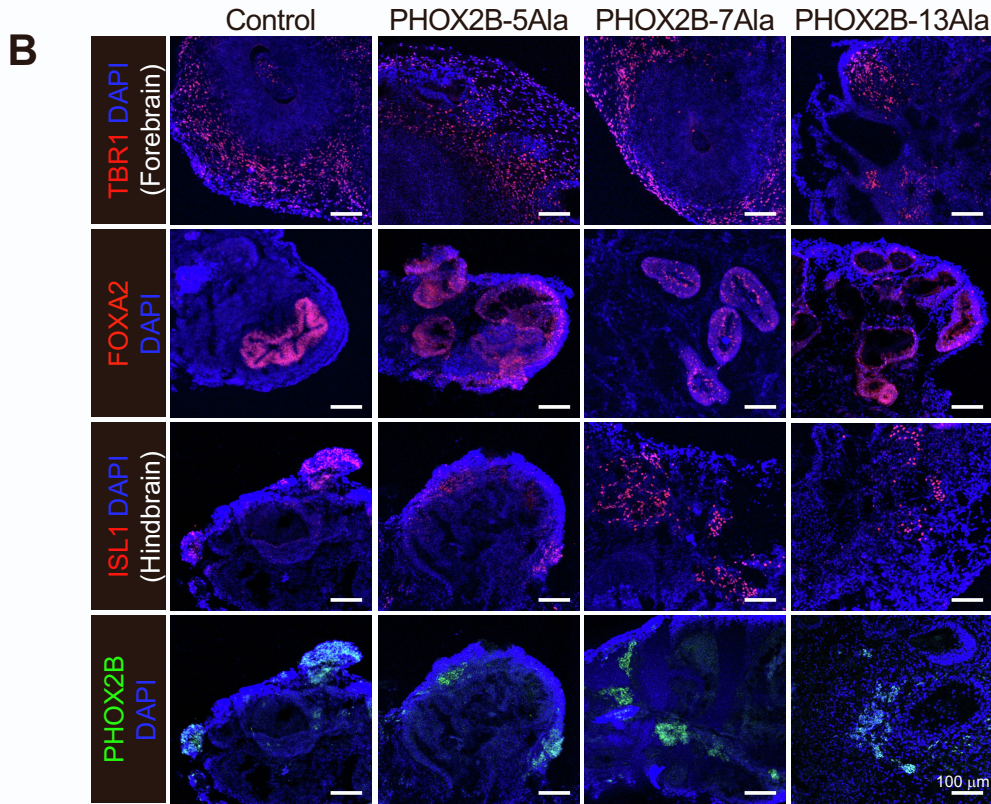
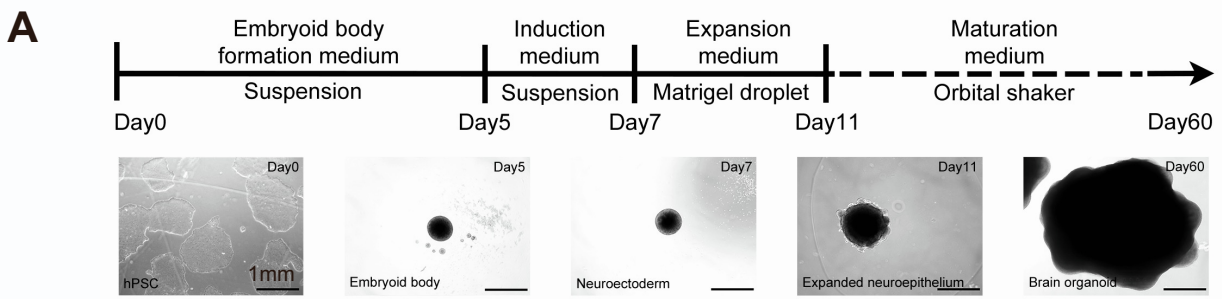


Fig. S4 Generation of unguided brain organoids (HCOs) from the control and PHOX2B-PARM mutant hPSCs. (A) Schematic shows the derivation of HCOs from hPSCs. Representative phase-contrast images of each stage are shown. **(B)** Immunostaining of PHOX2B and markers of forebrain (TBR1), midbrain (FOXA2) and hindbrain (ISL1) in the day-60 HCOs derived from the control and the PHOX2B-PARM mutants. **(C)** Representative images of day-60 HCOs derived from the control and PHOX2B-PARM mutants, immuno-stained with PHOX2B and 5-HT, representing the respiratory center-like regions (outlined by the yellow dashed lines). The inset in the bottom panel is an enlargement of the white squared region in the image. Bar chart showing the percentage area of respiratory center-like region in the control and PHOX2B-PARM mutant HCOs. One-way ANOVA. NS, non-significant.

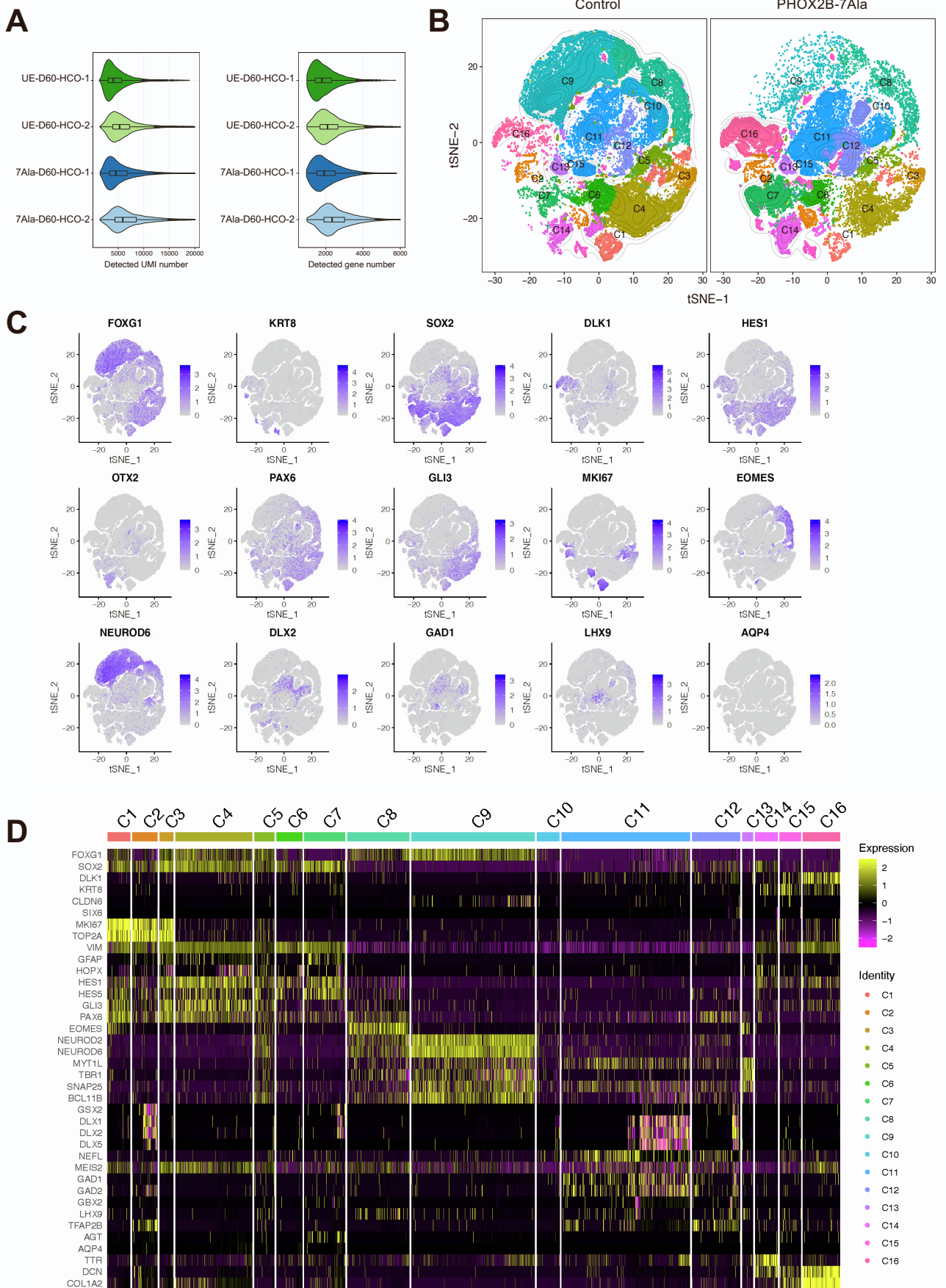


Fig. S5 Quality control and overall characteristics of the scRNA-seq dataset. (A) The number of detected UMI and gene numbers in four HCO samples. (B) Distribution of the 16 clusters from the control and PHOX2B-7Ala mutant HCOs in *t*-SNE plot (colored by clusters). (C) Canonical markers expressed in 16 clusters in the integrated HCO cells, colored by expression level. (D) Heatmap showed the unique markers of each cluster.

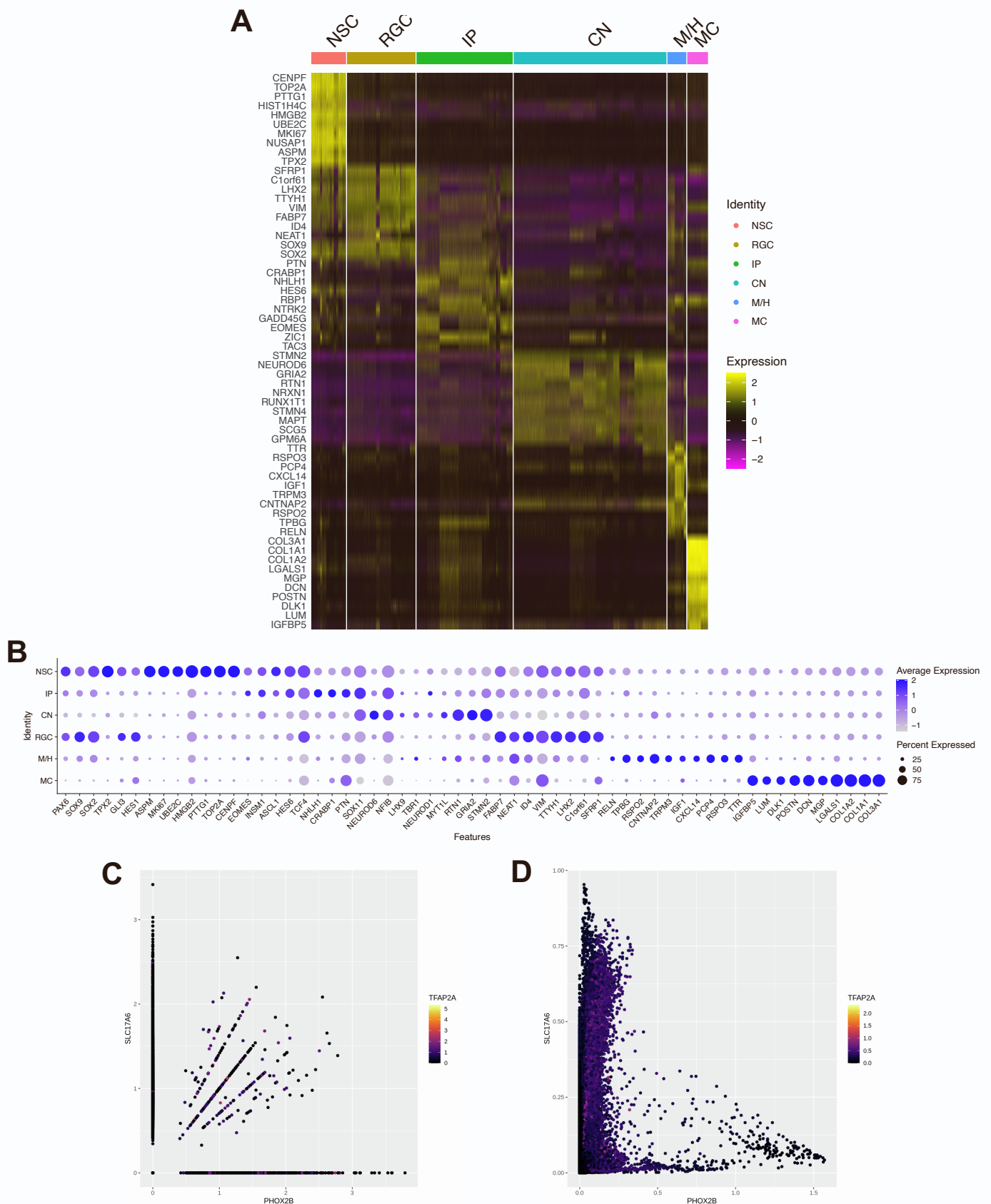


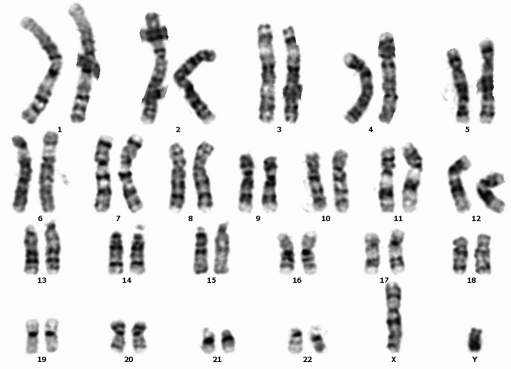
Fig. S6 Fine annotations of 16 clusters into 6 functional cell types and imputation analysis. (A) Heatmap showing the unique markers of 6 main cell types in the day-60 HCOs. NSC, neural stem cells; RGC, radial glial cells; IP, intermediate progenitors; CN, cortical neurons; M/H, mid/hindbrain cells; MC, mesenchymal-like cells. (B) Dot-plot showing the top key markers expressed in each cell type. Color of dot indicates the relative expression and size of dot indicates the percentage of cells expressing the gene. Expression of *PHOX2B* (C) before and (D) after imputation.

A

Clinical features:
<ul style="list-style-type: none"> • Central hypoventilation syndrome (CCHS) • Short Hirschsprung disease (S-HSCR) • Marcus gunn phenomenon • Global developmental delay
Genotype:
PHOX2B-7Ala-PARM t(11;22) (q23;q11.2)

B

46,XY,t(11;22) (q23;q11.2)

**C**

	CCHS-HSCR Fibroblast	15C11- hPSC
NANOG promoter	● ○ ○ ○	○ ○ ○ ○
	● ● ● ○	○ ○ ○ ○
	○ ● ● ○	○ ○ ○ ○
	● ● ● ○	○ ○ ○ ○
	● ● ○ ○	○ ○ ○ ○
	● ● ● ○	○ ○ ○ ○
	● ● ● ○	○ ○ ○ ○
	● ● ● ○	○ ○ ○ ○
	● ● ● ○	○ ○ ○ ○
	● ● ● ○	○ ○ ○ ○

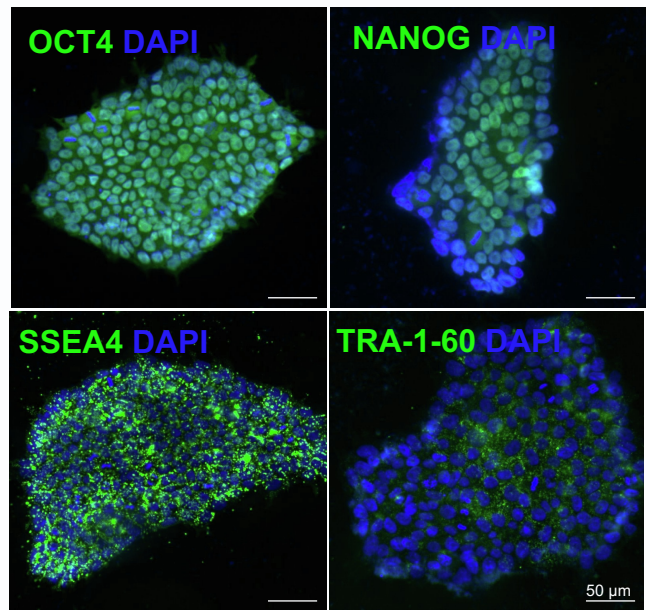
D

Fig. S7 Establishment and characterization of a CCHS-hPSC (15C11) line. (A) Table summarized the clinical features and genotype of the CCHS patient. (B) Karyotype of 15C11 hPSC. (C) Promoter of *NANOG* is unmethylated in the 15C11 hPSC. (D) Immunocytochemistry showing the expression of stem cell markers in the 15C11 hPSC. Scale bars: 50 μ m.

Supplementary Materials and methods

Human induced pluripotent stem cells (hPSCs)

UE02302 control hPSC line was kindly provided by Dr. Guangjin Pan (Guangzhou Institutes of Biomedicine and Health, Chinese Academy of Sciences, China)¹. A CCHS patient hPSC line (15C11) was generated from skin fibroblast of a CCHS patient with episomal reprogramming vector carrying the 4 reprogramming factors (*Oct4*, *Klf4*, *Sox2* and *c-Myc*) as described previously^{2,3}. The study was approved by the Institutional Review Board of The University of Hong Kong and the Hospital Authority (UW 13-419). All the hPSC lines were maintained in Matrigel (Corning, 354277)-coated 6-well culture plates with mTeSR1 medium (STEMCELL Technologies, 85850) in 37 °C humidified 5% CO₂ incubator. The hPSCs were regularly passaged by treating with Dispase (STEMCELL Technologies, 07923) and the culture medium was changed daily.

Plasmid constructions

The human codon-optimized Cas9 expression plasmid was obtained from Addgene (44720). Two guide RNAs (gRNA) were designed using the CRISPR design tool (<http://crispr.mit.edu>) to target the 20-Ala polyalanine tract in exon 3 of *PHOX2B* (PHOX2B-gRNAa: 5'-CCT TAG TGA AGA GCA GTA TGT TC-3'; PHOX2B-gRNAb: 5'-AAG AGC AGT ATG TTC TGA TCT GG-3'). The gRNA plasmid (Addgene, 41824) was linearized with *Afl*III and the gRNA targeting sequence (see Supplementary Table 1) was cloned into gRNA plasmid using Gibson Assembly (New England Biolabs, E2611) according to Church's lab protocol⁴.

The donor plasmid, pHR-PHOX2B-L-2A-EGFP, containing the homology arms spanning a region from chr4:41746593-41745806 (GRCh38.p13) and a puromycin selection cassette designed for *PHOX2B* targeting, is a generous gift from Dr. Yohan Oh (Johns Hopkins University School of Medicine, Baltimore). For construction of *PHOX2B-PARM* mutant donor plasmids containing different length of PARMs, oligos with additional Ala repeats were annealed and extended using Q5 High-fidelity DNA Polymerase (New England Biolabs, M0491). Annealed double-stranded oligos containing the desired additional Ala repeats (+5Ala, +7Ala and +13Ala) together with a 189-bp PCR fragment containing the 3'-end of the polyalanine tract region were subcloned into the ~8kb PCR fragment of the wild-type *PHOX2B* donor plasmid backbone (all designed with ~40bp overlapping sequences at each end) by

Gilson Assembly according to manufacturer's protocol. DNA sequence of all the *PHOX2B-PARM* mutant donor plasmids were confirmed by Sanger sequencing.

Generation of PHOX2B-PARM mutant hPSC cell lines

The CRISPR-Cas9 system⁵ was used to target the exon3 of *PHOX2B* allele (after stop codon) in the UE02302 control hPSCs. The hPSCs were transfected with the mutant *PHOX2B-PARM* donor plasmids together with the gRNA constructs and a Cas9 nickase expression plasmid using Human Stem Cell Nucleofactor Kit 2 (Lonza, VPH-5022). The transfected cells were selected for 7 days in 0.2 $\mu\text{g ml}^{-1}$ Puromycin and the Puromycin-resistant clones were isolated and passaged twice before genotyping. The targeted region of *PHOX2B* gene was genotyped by using the primers listed in Supplementary Table 1 to confirm the site-specific insertion of PARMs using Sanger sequencing. The mutant hPSC clones with the confirmed PARM insertion were expanded for further assays.

Correction of PHOX2B mutation in the CCHS-hPSC line

The strategy for the correction of patient-specific *PHOX2B* mutation was similar to the protocol described above except for the use of the wild-type *PHOX2B* donor plasmid instead of the mutant *PHOX2B-PARM* donor plasmids. In brief, CCHS (15C11) hPSCs were transfected with the wild-type *PHOX2B* donor plasmid, the gRNA constructs and a Cas9-D10A nickase expression plasmid using Human Stem Cell Nucleofactor Kit 2. Selection and screening of positive clones were performed as described above.

Generation of human cerebral organoids (HCOs) from hPSCs

HCOs were generated from hPSCs using a commercially optimized kit, STEMdiff Cerebral Organoid Kit (STEMCELL Technologies, 08570) following the manufacturer's protocol and previously described protocols^{6,7} with modifications. First, to generate embryoid body (EB) from hPSCs for the formation of HCOs, hPSCs were washed with DPBS (Cytiva, SH30028.03) and treated with 0.5 mM EDTA solution in DPBS for 4 min at 37 °C. After removing the EDTA solution, the cells were dissociated into single cell suspension by treating with Accutase (STEMCELL Technologies, 07922) for 4 min at 37 °C. The cells were pelleted by centrifugation for 5 minutes at $270 \times g$ at room temperature and then resuspended with EB

Formation Medium with ROCK inhibitor Y-27632 (10 μM). 9,000 cells were transferred to each well of 96-well round bottom ultra-low attachment plate (Corning, 7007) and kept undisturbed overnight in 37 °C incubator for the EB formation. The cells were marked as day 0 at this stage. At day 2 and 4, the EBs were fed with additional 100 μl EB Formation Medium per well. On day 5, one EB was transferred to each well of 24-well ultra-low attachment plate (Corning, 3473) with 500 μl Induction Medium to induce the formation of neuroepithelia. On day 7, the organoids were embedded in Matrigel and transferred to 6-well ultra-low attachment plate (Corning, 3471) for further expansion in Expansion Medium. On day 11, the medium was replaced with Maturation Medium and the 6-well plate (with 6-8 organoids per well) was kept shaking at 75 r.p.m. with an orbital shaker installed inside the incubator. The medium was changed every 3-4 days until day 60, when the organoids were collected.

Generation of brainstem organoids (HSBOs) from hPSCs

To generate HSBOs, hPSCs were dissociated into single cell suspension by treating with 0.5 mM EDTA solution in DPBS and then Accutase as described above. 2.7×10^6 cells were seeded to a well of AggreWell800 24-well plate (STEMCELL Technologies, 34815) which contained 300 microwells per well (i.e. 9,000 cells per microwell). The cells were kept in mTeSR1 with 10 μM Y-27632 overnight in 37 °C incubator for the spheroid formation and they were marked as day 0 at this stage. At day 1, the spheroids from one well of AggreWell800 were split into 3 wells of 6-well ultra-low-attachment plate containing Neural Induction Medium (DMEM/F12, 1% N2 supplement (v/v), 1% GlutaMAX supplement (v/v), 1% MEM-NEAA (v/v) and 1 $\mu\text{g ml}^{-1}$ Heparin) supplemented with BMP inhibitor LDN-193189 (1 μM) and TGF- β inhibitor SB431542 (10 μM). From day 3 to 6, the organoids were incubated in Neural Differentiation Medium (NDM) containing DMEM/F12 and Neurobasal Medium in 1:1 ratio with 0.5% N2 supplement (v/v), 1% B27 supplement without Vitamin A (v/v), 1% GlutaMAX (v/v), 0.5% MEM non-essential amino acids (NEAA), 2.5 $\mu\text{g ml}^{-1}$ insulin, 49.5 μM β -mercaptoethanol and 1% Penicillin-Streptomycin (Pen-Strep) (v/v). LDN-193189 (1 μM), SB431542 (10 μM) and SHH agonist SAG (1 μM) were added to NVM at day 3 to 6. Starting from day 3, the organoids were kept shaking at 90 r.p.m. with an orbital shaker installed inside the incubator. From day 6 to 12, the organoids were maintained in NDM with SAG (1 μM), WNT agonist CHIR99021 (3 μM) and retinoic acid (RA) (1 μM) and the medium was changed every 2-3 days. From day 12 onwards, the organoids were maintained in Neural Maturation Medium (NMM) (same recipe as NDM but with B27 containing Vitamin A) supplemented

with 20 ng ml⁻¹ BDNF, 20 ng ml⁻¹ GDNF, 50 nM dibutyryl-cAMP and 200 μM ascorbic acid. The medium was changed every 3-4 days until day 60, when the organoids were collected. The suppliers and catalog numbers of the media and supplements used for the preparation of culture media were listed in Supplementary Table 1.

Multielectrode array (MEA) analysis

Day 60 HBSOs were dissociated with Papain Dissociation System (Worthington, LK003150) following the manufacturer's protocol. In brief, the HBSOs were digested with the papain solution in 37 °C incubator for 30 min with continuous shaking at 90 r.p.m. and then triturated with P1000 pipette. The triturated HBSOs were further digested in 37 °C incubator for an additional 10 min and then filtered through 40 μm cell strainer (Corning, 352340) to remove undigested cell debris. The dissociated cells were collected by centrifuging at 300 × g for 5 min at room temperature. The cells were then resuspended with DNase/ovomuroid inhibitor solution to stop the digestion. The cells were centrifuged at 300 × g for 5 min at room temperature and resuspended in BrainPhys Neuronal Medium (STEMCELL Technologies, #05790) supplemented with 0.5% N-2 supplement (v/v), 1% B-27 supplement (v/v), 1% GlutaMAX (v/v), 0.5% NEAA, 2.5 μg ml⁻¹ insulin, 20 ng ml⁻¹ BDNF, 20 ng ml⁻¹ GDNF, 50 nM dibutyryl-cAMP, 200 μM ascorbic acid, 49.5 μM β-mercaptoethanol and 1% (v/v) Pen-Strep. Five-microliter cell suspension with 1 × 10⁵ cells and 10 μg ml⁻¹ laminin was seeded into each well of 24-well CytoView MEA plate (Axion Biosystems, M384-tMEA-24W) pre-coated with 0.1% polyethylenimine (PEI) (Sigma-Aldrich, P3143) and maintained in 37 °C humidified 5% CO₂ incubator for at least 2 weeks before MEA analysis. The culture medium was changed every 3-4 days. MEA recordings were measured at 37 °C with 5-8% CO₂ in a Maestro Edge MEA System (Axion Biosystems) to detect spontaneous firing of spikes. The MEA plate was pre-equilibrate in the MEA system for at least 5 min before measurement and each treatment was recorded for 5-10 min to calculate the mean spike firing rate. For the pharmacological experiment, retigabine (Selleckchem, S4733) (10 μM) was applied to plate immediately before recording. The MEA recordings were analyzed using the Neural Module of AxIS Navigator 1.5 software and the Neural Metric Tool software (Axion Biosystems). The mean spike firing rate of each MEA recording was normalized with the first MEA recording undertaken in 5% CO₂ or 8% CO₂ condition to calculate the fold change.

Quantitative RT-PCR (qPCR)

Total RNA from HCOs and HBSOs were extracted by RNeasy Mini Kit (Qiagen) and the RNA concentrations were determined by Nanodrop 1000 Spectrophotometer (Thermo Fisher Scientific). The RNA was then reverse-transcribed to cDNA using HiScript III All-in-one RT SuperMix (Vazyme, R333-01). For real-time qPCR, cDNA samples were amplified by Luna Universal qPCR Master Mix (New England BioLabs, M3003) using specific primer pairs with PCR profiles of 95 °C (1 min) followed by 45 cycles of 95 °C (15 s) and 60 °C (30 s). Fluorescence was measured by ViiA 7 Real-Time PCR System (Thermo Fisher Scientific) at the end of each cycle. Each individual sample was assayed in triplicate and gene expression was normalized with *GAPDH* expression. The primers for qPCR analysis were listed in Supplementary Table 2.

Western blot

To extract proteins from HBSOs, HBSOs were lysed with Cell Lysis Buffer (1X) (Cell Signaling Technology, #9803) with PhosSTOP (Roche), Complete protease inhibitor cocktails (Roche) and 0.1 mM phenylmethylsulfonyl fluoride (PMSF) for 30 min on ice with vortex at intervals. The lysates were centrifuged at $10,000 \times g$ at 4 °C and the supernatant was collected. The protein extracts were separated by 12% SDS-PAGE and transferred to Immobilon-P PVDF membrane (Millipore, IPVH00010) using Trans-Blot® SD Semi-Dry Transfer Cell (Bio-Rad). The membrane was briefly washed with TBST and then blocked with blocking solution for 1 h at room temperature. After blocking, the membrane was incubated with 1:1000 rabbit anti-PHOX2B antibody (Abcam, ab) or 1:20,000 mouse anti-Actin antibody (Millipore, MAB1501) diluted in blocking solution at 4 °C overnight. The membrane was washed with TBST thrice for 10 min and then incubated with 1:2000 goat anti-rabbit immunoglobulins-HRP (Dako, P044801) or 1:5000 anti-mouse immunoglobulins-HRP (Dako, P044701) diluted in blocking solution for 1 h at room temperature. After washing thrice with TBST for 10 min, the HRP signals were detected using WesternBright ECL (Advansta, K-12045-D50).

Immunofluorescence

The HCOs and HBSOs were fixed with 4% (w/v) paraformaldehyde (PFA) in PBS at room temperature for 1-2 h or 4 °C overnight. After washing with PBS for 5 min thrice, the samples were dehydrated with 15% (w/v) sucrose in PBS and then with 30% (w/v) sucrose in PBS at 4 °C overnight. The dehydrated samples were embedded in Tissue-Tek O.C.T. Compound (Sakura, 4583) and frozen on dry ice. The frozen blocks were stored at -80 °C until sectioning. Sections with 10-20 μm -thickness were cut using Leica CM3050 S cryostat and mounted on

Superfrost Plus Adhesion Slides (Thermo Fisher Scientific, J1800AMNZ). The frozen sections were kept at -20 °C for storage. The frozen sections were warmed at 37 °C for 10-30 min before IF procedures and washed with PBS for 5 min twice with gentle shaking. The sections were blocked with 5% (v/v) donkey serum in PBS with 0.1% (v/v) Triton X for 1 h at room temperature and then incubated with primary antibodies at 4 °C overnight. After washing with PBS for 10 min thrice, the sections were incubated with respective secondary antibodies for 2 h at room temperature. After washing with PBS for 10 min thrice, the stained cells were mounted with ProLong Diamond Antifade Mountant with DAPI (Thermo Fisher Scientific, P36971). The primary and secondary antibodies used for IF and ICC were listed in Supplementary Table 3. All the fluorescence images were acquired by Carl Zeiss LSM800 or LSM900 confocal microscope.

Droplet-based single-cell RNA-sequencing (scRNA-seq)

HBSOs and HCOs were harvested at day 60 and HBSOs were digested with Papain Dissociation System (Worthington) as described above while HCOs were digested with Accutase for 30 min at 37 °C with agitation. The HCOs were dissociated by pipetting every 10 min during digestion. All the dissociated cells were then filtered with 40 µm cell strainer and resuspended in 2% (v/v) FBS in DPBS in a density of 1×10^7 cells ml⁻¹. The viable cells were labeled with 7-AAD (5 µl per 10⁶ cells; BD Biosciences, 559925) for at least 10 min on ice. After filtering through 35 µm cell strainer, the cells negative for 7-AAD were gated and sorted with BD FACSAria III Cell Sorter using purity mode with purity $\geq 99\%$. The FACS-sorted cells were then subjected to droplet-based scRNA-seq using Chromium Single Cell platform and Single Cell 3' Library Kits (10x Genomics) in Centre of PanorOmic Science (CPOS), The University of Hong Kong. In brief, cells were encapsulated into Gel Beads-in-emulsion (GEMs) by the 10X Chromium Single Cell Controller, followed by reverse transcription and library preparation to become a pool of cDNA libraries. Libraries were then purified and sequenced on an Illumina™ NextSeq 500 according to the manufacturer's protocol.

Pre-processing of droplet-based scRNA-seq data

Cellranger toolkit (version 3.0) provided by 10X Genomics were used to perform the reads de-multiplexing and alignment. unique molecular identifier (UMI) were counted by aligning to the human hg38 transcriptome. For the quality control, only cells with more than 800 detected genes were retained. Genes expressed in more than 10 cells were kept for further analysis.

Clustering and marker identification were performed by the Seurat R package¹¹. The integrative analysis of the public datasets was also performed by Seurat.

Dimensionality reduction and cell clustering

The R package Seurat (version 3.1.4)¹² implemented in R (version 3.6.2) were used to perform dimensional reduction analysis. The “NormalizeData()” function from Seurat was used to normalize the raw counts, and the scale factor was set to 200,000, then followed by “FindVariableFeatures()” with default parameters to calculate highly variable genes for each sample. After performing “JackStraw()”, which returned the statistical significance of PCA (Principal component analysis) scores, we selected 20 significant PCs to conduct dimension reduction and cell clustering. Then, cells were projected in 2D space using *t*-SNE (*t*-distributed Stochastic Neighbor Embedding) with default parameters.

Single cell data integration and batch effect correction

To account for batch effect among different samples, we used “FindIntegrationAnchors()” in the Seurat package to remove batch effect and merge samples to one object. In detail, the top 4,500 genes with the highest expression and dispersion from each sample were used to find the integration anchors, and then the computed anchor set was applied to perform dataset integration.

Organoid comparison

Human brainstem organoids (HBSOs) and human cerebral organoids (HCOs) were derived from the sequencing data in this article, while human cortical organoids (hFBCOs, GSE137941), human midbrain organoids (hMBOs, GSE133894), human thalamic organoids (hThaOs, GSE122342) and human arcuate organoids (hARCOs, GSE164102) were downloaded from Gene Expression Omnibus (GEO) database. Raw count matrix of UMI were downloaded and normalized by NormalizeData() function in Seurat R package. Cells from each organoid models were pooled together to construct “pseudo-bulk” expression for each organoid. Similarities between different organoids were estimated by Spearman correlation.

Reference-based cell annotation

Developing¹³ and adolescent¹⁴ mouse brain atlas were downloaded from <http://mousebrain.org/>. Developing and adolescent neuron, glia, OPC, radial glia, Schwann cell and astrocyte located at hindbrain were extracted for comparison with our HBSO scRNA-seq dataset. Reference-based cell annotation was performed by Seurat R package. In brief, raw

count matrix were normalized and scaled first. Then, FindTransferAnchors() function was applied to find shared anchors between datasets. Finally, MapQuery() was used to project query dataset (HBSOs) to reference datasets (developing and adolescent mouse brain cells). Thus, original cell type labels were transferred to HBSOs datasets based on the overall expression patterns of genes and cells in HBSOs were classified to six main cell types (neuron, glia, OPC, radial glia, Schwann cell and astrocyte).

Human cerebral organoids from public scRNA-seq datasets ¹⁵ were downloaded from <https://www.ebi.ac.uk/arrayexpress/experiments/E-MTAB-7552/>. 2-month-old human cerebral organoids were extracted and overlaid with our HCO cells for comparison analysis. Potential technical and batch effects were removed by Seurat software¹². The sixteen unbiased clusters were further classified into six cell types, including neural stem cells (NSC), radial glia cells (RGC), intermediate progenitors (IP), cortical neurons (CN), midbrain/hindbrain (M/H) and mesenchymal-like cells (MC) based on the expression of canonical markers and the cell annotation from the public datasets.

Marker-based neuronal subtype annotation

Neuronal cells in HBSOs were further classified into four main neuron subtypes (Cholinergic, Serotonergic, GABAergic and Glutamatergic) and two novel subtypes (PHOX2B^{Low} and PHOX2B^{High}) based on the canonical marker genes as stated in previous literature ¹⁶. Gene signature expression of each subtype was calculated to confirm the identity of neuronal cells.

Lineage cladogram construction

Pseudo-bulk expression (average expression) of each cell type was calculated. Pairwise Euclidean distances were calculated among cell types. Neighbor-joining (NJ) tree was estimated based on the distance matrix. ggtree R package ¹⁷ was used to visualize the lineage cladogram.

RNA velocity analysis

Velocyto (<http://velocyto.org/velocyto.py/index.html>) was used to calculate spliced and unspliced matrix from bam files that derived from cellranger pipeline. Then, scVelo ¹⁸ was applied for RNA velocity analysis in single cells.

Single cell trajectory analysis

Single cell trajectory analysis was performed by PCA algorithm using *PHOX2B*⁺ cells.

Identification of differentially expressed genes and pathway enrichment analysis

To identify unique differentially expressed genes (DEGs) among each cluster, the “FindAllMarkers()” function from Seurat was used and non-parametric Wilcoxon rank sum tests were set to evaluate the significance of each individual DEG. The DEG analysis between mutant and control based on single-cell expression data was performed using monocle (version 2.14.0) R package¹⁹. The DEGs with adjusted *P*-value less than 0.05 and Log₂ Fold Change (log₂FC) larger than 0.5 were thought to be significant and used in downstream analysis. Gene ontology (GO) term enrichment analyses were performed using clusterProfiler (version 3.14.3) R package²⁰. Terms that had an adjusted *P*-value < 0.05 was defined as significantly enriched.

Pathway score analysis

In order to measure the activity of whole pathways between samples at transcriptome level, we applied a simple additive model that ignore the interactions between genes to estimate the overall expression level of the pathways. The genes involved in GO:0007389 (pattern specification process) in GO database were used to evaluate the overall changes of the key biological processes.

Gene regulatory network (GRN) analysis

Single cell regulatory network inference and clustering (SCENIC, version 1.1.2)²¹ was used to infer transcription factor networks active using scRNA-Seq data. Analysis was performed using default and recommended parameters as directed on the SCENIC vignette (<https://github.com/aertslab/SCENIC>) using the hg38 RcisTarget database. Kernel density line histograms showing differential AUC score distribution across conditions were plotted with ggplot2 v.3.1.1 using the regulon activity matrix (‘3.4_regulonAUC.Rds’, an output of the SCENIC workflow) in which columns represent cells and rows the AUC regulon activity. Fold-change (FC) difference between median AUC values was calculated and the highest changed TFs were plotted.

Differential co-expression analysis

To predict PHOX2B activated and repressed target genes, we applied a three-step strategy to obtain the target genes of PHOX2B during progenitor-to-neuron transition. In the first step, we identified the significantly correlated genes to PHOX2B which represented the genes that had

strong regulatory relationships with PHOX2B. In the second step, we utilized the differential expression profile between control and mutant to filter out the genes whose expression levels were not significantly disrupted by PHOX2B. Finally, to confine the genes to be the actual targets of PHOX2B, a public ChIP-seq dataset designed for PHOX2B from a similar cell state (neuronal progenitor) in Cistrome database ²² was utilized to obtain the direct/indirect binding genes of PHOX2B. Activated and repressed target genes were determined by the positive/negative correlation and up/down-regulation of the differential expression, respectively. In addition, TF motif enrichment analysis by FIMO tool ²³ of MEME suite ²⁴ was used to cross-validate the predicted activated targets of PHOX2B.

Imputation

Markov affinity-based graph imputation of cells (MAGIC)²⁵ was used to denoise the cell count matrix and fill in missing transcripts. The expression of PHOX2B could be well-recovered and most of the PHOX2B+ cells were found in cell clusters inferred to be less mature progenitors (IP) or more mature neurons (CN), and few fell into NSC in control HCOs.

Image analysis and statistical analysis

Cell numbers in immunostaining or immunocytochemistry were quantified using “Cell Counter” or “Analyze Particles” modules in Fiji ImageJ software ^{26,27}. Statistical analysis was performed with the software Prism 9.0 (GraphPad Software). Unless otherwise noted, the data were expressed as mean \pm SEM. Two-tailed unpaired Student’s *t*-test was used for comparisons involving two groups. One-way ANOVA, followed by Turkey’s multiple comparison test, was used for comparisons involving more than two groups. Probability values $P < 0.05$ were considered as statistically significant.

Supplementary Table 1. List of media and supplements used for culture of hPSCs, HBSOs, HCOs, hENCCs and ENS neurons.

Media and supplements	Applications	Suppliers	Catalog#
mTesR1 medium	hPSCs, HBSOs	STEMCELL Technologies	85850
STEMdiff Cerebral Organoid Kit	HCOs	STEMCELL Technologies	08570
BrainPhys Neuronal Medium	HBSOs (MEA)	STEMCELL Technologies	05790
DMEM/F-12	hiPSCs, HBSOs	Thermo Fisher Scientific	11330032
DMEM/F-12 (with GlutaMAX supplement)	hENCCs and ENS neurons	Thermo Fisher Scientific	10565018
KnockOut DMEM	hENCCs	Thermo Fisher Scientific	10829018
Neurobasal Medium	HBSOs, hENCCs and ENS neurons	Thermo Fisher Scientific	21103049
KnockOut Serum Replacement (KOSR)	hENCCs	Thermo Fisher Scientific	10828028
B-27 Supplement	HBSOs, hENCCs and ENS neurons	Thermo Fisher Scientific	17504044
B-27 supplement without Vitamin A	HBSOs	Thermo Fisher Scientific	12587010
N-2 Supplement	HBSOs, hENCCs and ENS neurons	Thermo Fisher Scientific	17502048
Insulin	HBSOs, hENCCs and ENS neurons	Thermo Fisher Scientific	12585014
GlutaMAX supplement	HBSOs	Thermo Fisher Scientific	35050061
L-Glutamine	hENCCs	Thermo Fisher Scientific	25030081
MEM Non-Essential Amino Acids (NEAA)	HBSOs, hENCCs and ENS neurons	Thermo Fisher Scientific	11140050
β -mercaptoethanol	HBSOs, hENCCs and ENS neurons	Thermo Fisher Scientific	21985023
Penicillin-Streptomycin (Pen-Strep)	HCOs, HBSOs, hENCCs and ENS neurons	Thermo Fisher Scientific	15140122
Heparin	HBSOs	Sigma-Aldrich	H3149
FGF-2	hENCCs and ENS neurons	Peprtech	100-18B
Y-27632	hPSCs, HCOs, HBSOs, hENCCs and ENS neurons	Tocris	1254
LDN-193189	HBSOs, hENCCs and ENS neurons	Reprocell	04-0074
SB431542	HBSOs, hENCCs and ENS neurons	Abcam	ab120163
SAG	HBSOs	Sigma-Aldrich	SML1314
IWR-1-endo	HBSOs	Abmole	M2782

CHIR99021	HBSOs, hENCCs and ENS neurons	Reprocell	04-0004
Retinoic acid (RA)	HBSOs, hENCCs and ENS neurons	Abcam	ab120728
BDNF	HBSOs and ENS neurons	Peprtech / Qkine	450-02 / Qk050
GDNF	HBSOs and ENS neurons	Peprtech / Shenandoah	450-10 / 100-02
NT-3	hENCCs and ENS neurons	Peprtech	450-03
β -NGF	hENCCs and ENS neurons	Peprtech	450-01
Dibutyryl-cAMP	HBSOs, hENCCs and ENS neurons	Sigma-Aldrich	D0260
Ascorbic acid	HBSOs, hENCCs and ENS neurons	Sigma-Aldrich	A4034

Supplementary Table 2. List of RT-PCR primers used in this study.

Gene	Oligo sequence (5' to 3')	Applications	T _m (°C)	Product size (bp)
<i>HOXA2</i>	Forward: CGTCGCTCGCTGAGTGCCTG Reverse: TGTCGAGTGTGAAAGCGTCGAGG		63.3 61.1	92
<i>HOXB1</i>	Forward: GAGCTTTGCACCGGCCTAT Reverse: CTTCATCCAGTCGAAGGTCCG		58.1 57.4	103
<i>HOXB2</i>	Forward: CCTAGCCTACAGGGTTCTCTC Reverse: CACAGAGCGTACTGGTGAAAAA		56.1 55.4	79
<i>GBX2</i>	Forward: ACGTCAGCAGGTTTCGCTATC Reverse: AGCTGGGCTGTGACTTTGTT		57.2 57.3	166
<i>OTX2</i>	Forward: AGTCGAGGGTGCAGGTATG Reverse: GGCCACTTGTCCACTCTCT		56.6 57.1	153
<i>PAX7</i>	Forward: CAAACACAGCATCGACGGC Reverse: CTTCAGTGGGAGGTCAGGTTC		57.3 57.2	91
<i>OLIG3</i>	Forward: TCATGCTCACCAGCTCCCT Reverse: CCCCATAGATCTCGCCAAC		58.7 57.6	58
<i>NGN1</i>	Forward: AAGACTTCACCTACCGCCC Reverse: GCGTGTGTGGAGCAAGT		56.9 58.6	76
<i>PHOX2B</i>	Forward: AAACTCTTCACGGACCACGG Reverse: CTCCTGCTTGCGAAACTTGG		57.4 56.8	222
<i>GAPDH</i>	Forward: CAAGAAGGTGGTGAAGCAGGC Reverse: GCCAAATTCGTTGTCATACCAGGA		58.7 57.6	184

Supplementary Table 3. List of antibodies used in this study.

Target antigens	Antibodies	Dilutions	Applications	Suppliers	Catalog#	RRID
Actin	Mouse monoclonal anti-Actin	1:20,000	WB	Sigma-Aldrich	MAB1501	AB_2223041
CD271 (LNGFR) (p75 ^{NTR})	Mouse anti-human CD271 (LNGFR), FITC	2 μ l per 10 ⁷ cells	FACS	Miltenyi Biotec	130-113-420	AB_2733631
CD57 (HNK1)	Mouse anti-human CD57, APC	1 μ l per 10 ⁷ cells	FACS	BD Biosciences	560845	AB_10563760
Cleaved Caspase-3 (C-Cas3)	Rabbit anti-Cleaved Caspase-3	1:200	IF	Cell Signaling Technology	9661	AB_2341188
Forkhead box A2 (FOXA2)	Mouse monoclonal anti-FOXA2 [7E6]	1:200	IF	Abcam	ab60721	AB_941632
Green fluorescent protein (GFP)	Sheep polyclonal anti-GFP	1:500	IF, ICC	Bio-Rad	4745-1051	AB_619712
Islet 1 (ISL1)	Rabbit monoclonal anti-ISL1 [EP4182]	1:200	IF	Abcam	ab109517	AB_10866454
Nanog Homeobox (NANOG)	Goat polyclonal anti-NANOG	1:500	ICC	R&D Systems	AF1997	AB_355097
Neurofilament (NF)	Chicken polyclonal anti-NF-L	1:500	ICC	Neuromics	CH22105	AB_2737102
Neuronal differentiation 6 (NEUROD6)	Rabbit polyclonal anti-MATH2/NEUROD6	1:200	IF	Abcam	ab85824	AB_10671651
NK2 Homeobox 2 (NKX2.2)	Mouse monoclonal anti-Nkx2.2	1:100	IF	DSHB	74.5A5	AB_531794
Octamer-binding transcription factor 4 (OCT4)	Goat polyclonal anti-Oct-3/4	1:100	ICC	Santa Cruz	sc-8629	AB_2167705
Orthodenticle homeobox 2 (OTX2)	Rabbit polyclonal anti-Otx1+Otx2	1:200	IF	Abcam	ab21990	AB_776930
Paired like homeobox 2B (PHOX2B)	Goat polyclonal anti-PHOX2B	1:200	IF, ICC	R&D Systems	AF4940	AB_10889846
Paired like homeobox 2B (PHOX2B)	Rabbit monoclonal anti-PHOX2B [EPR14423] – C-terminal	1:200	ICC, WB	Abcam	ab183741	AB_2857845
Protein gene product 9.5 (PGP9.5)	Rabbit monoclonal anti-PGP9.5 [EPR4118]	1:500	ICC	Abcam	ab108986	AB_10891773
Serotonin (5-HT)	Rat monoclonal anti-Serotonin [YC5/45]	1:200	IF	Abcam	ab6336	AB_449517
Sex-determining region Y-box 10 (SOX10)	Mouse monoclonal anti-SOX10	1:500	ICC	R&D Systems	MAB2864	AB_2195180
Sex-determining region Y-box 2 (SOX2)	Mouse monoclonal anti-SOX2	1:200	IF	R&D Systems	MAB2018	AB_358009

Stage-Specific Embryonic Antigen-4 (SSEA4)	Mouse monoclonal anti-SSEA-4	1:200	ICC	Sigma-Aldrich	MAB4304	AB_177629
T cell receptor alpha locus (TRA-1-60)	Mouse monoclonal anti-TRA-1-60	1:100	ICC	Sigma-Aldrich	MAB4360	AB_2119183
T-Box brain transcription factor 2 (TBR2)	Rabbit polyclonal anti-TBR2	1:200	IF	Abcam	ab23345	AB_778267
Tubulin beta 3 class III (TUJ1 or TUBB3)	Rabbit polyclonal anti-TUJ1	1:1,000	ICC	Abcam	ab18207	AB_444319
Tubulin beta 3 class III (TUJ1 or TUBB3)	Mouse monoclonal anti-TUJ1	1:1,000	IF, ICC	BioLegend	801202	AB_10063408
Tyrosine hydroxylase (TH)	Mouse monoclonal anti-TH	1:500	IF, ICC	Sigma-Aldrich	MAB318	AB_2201528
Vesicular glutamate transporter 2 (VGLUT2)	Guinea pig polyclonal anti-VGLUT2	1:1,000	IF	Sigma-Aldrich	AB2251-I	AB_2665454
Alexa Fluor® 488 Donkey-anti-goat IgG (H+L)		1:200	IF, ICC	Thermo Fisher Scientific	A11055	AB_2534102
Alexa Fluor® 488 Donkey-anti-mouse IgG (H+L)		1:200	IF, ICC	Thermo Fisher Scientific	A21202	AB_141607
Alexa Fluor® 488 Donkey-anti-rabbit IgG (H+L)		1:200	IF, ICC	Thermo Fisher Scientific	A21206	AB_2535792
Alexa Fluor® 488 Donkey-anti-sheep IgG (H+L)		1:200	IF, ICC	Thermo Fisher Scientific	A11015	AB_2534082
Alexa Fluor® 594 Donkey-anti-mouse IgG (H+L)		1:200	IF, ICC	Thermo Fisher Scientific	A21203	AB_141633
Alexa Fluor® 594 Donkey-anti-rabbit IgG (H+L)		1:200	IF, ICC	Thermo Fisher Scientific	A21207	AB_141637
Alexa Fluor® 594 Donkey-anti-rat IgG (H+L)		1:200	IF, ICC	Thermo Fisher Scientific	A21209	AB_2535795
Alexa Fluor® 594 Goat-anti-chicken IgY (H+L)		1:200	IF, ICC	Thermo Fisher Scientific	A11042	AB_2534099
Alexa Fluor® 647 Donkey-anti-mouse IgG (H+L)		1:200	IF, ICC	Thermo Fisher Scientific	A31571	AB_162542
Alexa Fluor® 647 Donkey-anti-rabbit IgG (H+L)		1:200	IF, ICC	Thermo Fisher Scientific	A31573	AB_2536183
Donkey anti-guinea pig IgG (H+L) highly cross-adsorbed, CF594		1:200	IF, ICC	Sigma-Aldrich	SAB4600096	AB_2728625
Goat anti-rabbit immunoglobulins-HRP		1:2,000	WB	Dako	P044801	AB_2617138
Rabbit anti-mouse immunoglobulins-HRP		1:5,000	WB	Dako	P04470	AB_2617137

Supplementary References

1. Xue Y, Cai X, Wang L, *et al.* Generating a non-integrating human induced pluripotent stem cell bank from urine-derived cells. *PLoS One.* 2013;8(8):e70573. doi:10.1371/journal.pone.0070573
2. Takahashi K, Okita K, Nakagawa M, Yamanaka S. Induction of pluripotent stem cells from fibroblast cultures. *Nat Protoc.* 2007-12-01 2007;2(12):3081-9. doi:10.1038/nprot.2007.418
3. Lai FP, Lau ST, Wong JK, *et al.* Correction of Hirschsprung-Associated Mutations in Human Induced Pluripotent Stem Cells Via Clustered Regularly Interspaced Short Palindromic Repeats/Cas9, Restores Neural Crest Cell Function. *Gastroenterology.* Jul 2017;153(1):139-153 e8. doi:10.1053/j.gastro.2017.03.014
4. Mali P, Yang L, Esvelt KM, *et al.* RNA-guided human genome engineering via Cas9. *Science.* Feb 15 2013;339(6121):823-6. doi:10.1126/science.1232033
5. Ran FA, Hsu PD, Wright J, Agarwala V, Scott DA, Zhang F. Genome engineering using the CRISPR-Cas9 system. *Nat Protoc.* Nov 2013;8(11):2281-2308. doi:10.1038/nprot.2013.143
6. Lancaster MA, Renner M, Martin CA, *et al.* Cerebral organoids model human brain development and microcephaly. *Nature.* Sep 19 2013;501(7467):373-9. doi:10.1038/nature12517
7. Lancaster MA, Knoblich JA. Generation of cerebral organoids from human pluripotent stem cells. *Nat Protoc.* Oct 2014;9(10):2329-40. doi:10.1038/nprot.2014.158
8. Lee G, Chambers SM, Tomishima MJ, Studer L. Derivation of neural crest cells from human pluripotent stem cells. *Nat Protoc.* Apr 2010;5(4):688-701. doi:10.1038/nprot.2010.35
9. Tang CS, Li P, Lai FP, *et al.* Identification of Genes Associated With Hirschsprung Disease, Based on Whole-Genome Sequence Analysis, and Potential Effects on Enteric Nervous System Development. *Gastroenterology.* Dec 2018;155(6):1908-1922 e5. doi:10.1053/j.gastro.2018.09.012
10. Lau ST, Li Z, Lai FPL, *et al.* Activation of Hedgehog Signaling Promotes Development of Mouse and Human Enteric Neural Crest Cells, Based on Single-Cell Transcriptome Analyses. *Gastroenterology.* Dec 2019;157(6):1556-1571 e5. doi:10.1053/j.gastro.2019.08.019
11. Butler A, Hoffman P, Smibert P, Papalexi E, Satija R. Integrating single-cell transcriptomic data across different conditions, technologies, and species. *Nat Biotechnol.* Jun 2018;36(5):411-420. doi:10.1038/nbt.4096
12. Hao Y, Hao S, Andersen-Nissen E, *et al.* Integrated analysis of multimodal single-cell data. *Cell.* Jun 24 2021;184(13):3573-3587 e29. doi:10.1016/j.cell.2021.04.048
13. La Manno G, Siletti K, Furlan A, *et al.* Molecular architecture of the developing mouse brain. *Nature.* 2021-08-05 2021;596(7870):92-96. doi:10.1038/s41586-021-03775-x
14. Zeisel A, Hochgerner H, Lönnerberg P, *et al.* Molecular Architecture of the Mouse Nervous System. *Cell.* 2018;174(4):999-1014.e22. doi:10.1016/j.cell.2018.06.021
15. Kanton S, Boyle MJ, He Z, *et al.* Organoid single-cell genomic atlas uncovers human-specific features of brain development. *Nature.* Oct 2019;574(7778):418-422. doi:10.1038/s41586-019-1654-9
16. Liu W, Venugopal S, Majid S, *et al.* Single-cell RNA-seq analysis of the brainstem of mutant SOD1 mice reveals perturbed cell types and pathways of amyotrophic lateral sclerosis. *Neurobiol Dis.* Jul 2020;141:104877. doi:10.1016/j.nbd.2020.104877
17. Yu G, Smith DK, Zhu H, Guan Y, Lam TTY. ggtree: an R package for visualization and annotation of phylogenetic trees with their covariates and other associated data. *Methods Ecol Evol.* 2017-01-01 2016;8(1):28-36. doi:10.1111/2041-210x.12628

18. Bergen V, Lange M, Peidli S, Wolf FA, Theis FJ. Generalizing RNA velocity to transient cell states through dynamical modeling. *Nature Biotechnology*. 2020/12/01 2020;38(12):1408-1414. doi:10.1038/s41587-020-0591-3
19. Qiu X, Mao Q, Tang Y, *et al.* Reversed graph embedding resolves complex single-cell trajectories. *Nat Methods*. Oct 2017;14(10):979-982. doi:10.1038/nmeth.4402
20. Yu G, Wang LG, Han Y, He QY. clusterProfiler: an R package for comparing biological themes among gene clusters. *OMICS*. May 2012;16(5):284-7. doi:10.1089/omi.2011.0118
21. Aibar S, Gonzalez-Blas CB, Moerman T, *et al.* SCENIC: single-cell regulatory network inference and clustering. *Nat Methods*. Nov 2017;14(11):1083-1086. doi:10.1038/nmeth.4463
22. Liu T, Ortiz JA, Taing L, *et al.* Cistrome: an integrative platform for transcriptional regulation studies. *Genome Biol*. Aug 22 2011;12(8):R83. doi:10.1186/gb-2011-12-8-r83
23. Grant CE, Bailey TL, Noble WS. FIMO: scanning for occurrences of a given motif. *Bioinformatics*. Apr 1 2011;27(7):1017-8. doi:10.1093/bioinformatics/btr064
24. Bailey TL, Johnson J, Grant CE, Noble WS. The MEME Suite. *Nucleic Acids Res*. Jul 1 2015;43(W1):W39-49. doi:10.1093/nar/gkv416
25. van Dijk D, Sharma R, Nainys J, *et al.* Recovering Gene Interactions from Single-Cell Data Using Data Diffusion. *Cell*. Jul 26 2018;174(3):716-729 e27. doi:10.1016/j.cell.2018.05.061
26. Schindelin J, Arganda-Carreras I, Frise E, *et al.* Fiji: an open-source platform for biological-image analysis. *Nature Methods*. 2012-07-01 2012;9(7):676-682. doi:10.1038/nmeth.2019
27. Schneider CA, Rasband WS, Eliceiri KW. NIH Image to ImageJ: 25 years of image analysis. *Nature Methods*. 2012-07-01 2012;9(7):671-675. doi:10.1038/nmeth.2089